

Article

Mixing in Two Types of Fluids Responsible for Some Carbonate-Hosted Pb–Zn Deposits, SW China: Insights from the Maoping Deposit

Lei Wang^{1,2}, Runsheng Han^{1,2,*}, Yan Zhang^{1,2,*} and Xiaodong Li^{1,2}

¹ Faculty of Land Resources Engineering, Kunming University of Science and Technology, Kunming 650093, China; wanglei880813@yeah.net (L.W.); 13474046051@163.com (X.L.)

² South-West Institute of Geological Survey, Geological Survey Center for Nonferrous Metals Resources, Kunming 650093, China

* Correspondence: 11301124@kust.edu.cn (R.H.); m15925201825@163.com (Y.Z.)

Abstract: Carbonate-hosted Pb–Zn deposits are of major economic importance. The Sichuan–Yunnan–Guizhou metallogenetic belt (SYGMB), located on the western margin of the Yangtze Block, comprises over 400 carbonated-hosted Pb–Zn deposits. However, ore-forming fluids recorded in these deposits have led to controversy regarding ore genesis. We investigated a fluid system for the Maoping deposit in the SYGMB, based on fluid inclusions, and H–O–He–Ar isotopic studies. The results showed that ore-forming fluids in the Maoping deposit are characterized by mixing of high-temperature and low-salinity metamorphic fluids and low-temperature and high-salinity basinal brines. The Precambrian basement is considered to produce metamorphic fluids, while the basinal brines are said to originate from the Youjiang Basin. The mineralization at the depositional site appears to reflect the coincidence of the metamorphic fluids, basinal brines, Carboniferous coal seams, and structural-stratigraphic traps. Regional-scale data show large-scale heterogeneity in fluid properties, including basinal brines, metamorphic fluids, and organic fluids. Furthermore, the data suggest a precipitation model for some high-grade Pb–Zn deposits in the SYGMB. These findings will contribute to an understanding of deposit types in the SYGMB.

Keywords: fluid inclusions; isotope; fluid mixing; carbonate-hosted Pb–Zn deposits; Southwest China



Citation: Wang, L.; Han, R.; Zhang, Y.; Li, X. Mixing in Two Types of Fluids Responsible for Some Carbonate-Hosted Pb–Zn Deposits, SW China: Insights from the Maoping Deposit. *Minerals* **2023**, *13*, 600. <https://doi.org/10.3390/min13050600>

Academic Editors: Yitian Wang, Changqing Zhang and Pierre Schiano

Received: 25 March 2023

Revised: 11 April 2023

Accepted: 24 April 2023

Published: 26 April 2023



Copyright: © 2023 by the authors. Licensee MDPI, Basel, Switzerland. This article is an open access article distributed under the terms and conditions of the Creative Commons Attribution (CC BY) license (<https://creativecommons.org/licenses/by/4.0/>).

1. Introduction

Most ore deposits form from aqueous fluids that are the main agent for the movement of mass in the crust [1]. These ore-forming fluids are commonly divided into meteoric water, sea water, basinal brines, metamorphic fluids, and magmatic fluids based on mainly their compositional variations related to different geological environments [2–4].

Carbonate-hosted Pb–Zn deposits play an important role in the supply of base metals to the world [5]. They occur in limestones or dolostones, with clearly epigenetic characteristics, and are generally not associated with or genetically related to igneous rocks [6–10]. This type of Pb–Zn deposit is best known for Mississippi-Valley-type (MVT) deposits [6,11–13]. In terms of fluid properties, the fluids associated with MVT deposits are distinct. It is widely accepted that MVT deposits precipitated from basinal brines, characterized by low temperatures (50° to 200 °C) and high salinities (10 to 30 wt.% NaCl eqv.) [13,14].

The Sichuan–Yunnan–Guizhou metallogenetic belt (SYGMB) in Southwest China comprises over 400 variably sized Pb–Zn deposits that are hosted in the late Ediacaran to early Permian carbonate sequences [15]. These Pb–Zn deposits contain total sulfur ore reserves of >200 Mt, with average grades of 10 wt.%–35 wt.% Pb + Zn [15–21]. Such extensive mineralization means the operation of a huge fluid system, with economic significance and academic value to attract the attention of many scholars. However, there are some debates on fluid properties and related deposit types in the SYGMB. Given that

these deposits are similar to typical MVT deposits, they have been generally classified as MVT deposits [22–25]. However, some of their geological characteristics (e.g., high grades, ore-controlled compressive structure, high temperatures, low salinities) differ from the typical MVT deposits, suggesting Huize-style [26–29] or SYG-type deposits [18,30]. In addition, deposits in the SYGMB have a close spatial relationship with Permian Emeishan flood basalts (EFBs), which leads to a consideration of magmatic fluids being associated with the Emeishan mantle plume for ore genesis [31].

The Maoping Pb–Zn carbonate-hosted deposit in the SYGMB has ~14 Mt of sulfide ores at mean grades of 6.1 wt.% Pb and 20.2 wt.% Zn [25,29]. We provide a detailed description of the geology in this deposit based on field investigations and petrographic observations. Fluid inclusions, traditional stable isotopes (H–O), and noble gas isotopes (He–Ar) are used to constrain the properties and sources of Maoping ore formation. The contribution of these data to the development of a genetic model for the Maoping deposit is emphasized. Previous data in the SYGMB are also presented to impact our understanding of carbonate-hosted Pb–Zn deposits in the SYGMB.

2. Regional Geology

The Sichuan–Yunnan–Guizhou metallogenic belt (SYGMB), located in the southwestern part of the Yangtze Block (Figure 1A), is limited by a triangular area bounded by the N-trending Anninghe–Lvzhijiang, SE-trending Mile–Shizong, and SW-trending Ziyun–Yadu faults (Figure 1B). The strata of the SYGMB are composed of basement metamorphic rocks, cover sedimentary rocks, and the Emeishan large igneous province (basalts); see Figure 1B. The basement comprises Archean (e.g., the Kangding group of ~3.3–2.9 Ga [32,33]), Mesoproterozoic (e.g., the Dongchuan group of ~1.7–1.5 Ga [34]), and Neoproterozoic (e.g., the Kunyang/Huili group of ~1.1–0.9 Ga [35,36]) metamorphic rocks. The cover overlies the basement by an angular unconformity. It consists of Ediacaran-to-Triassic sedimentary series, which are mainly marine carbonate rocks. The Late Permian Emeishan basalts (259 ± 3 Ma [37]) occupy a large part of the SYGMB (Figure 1B).

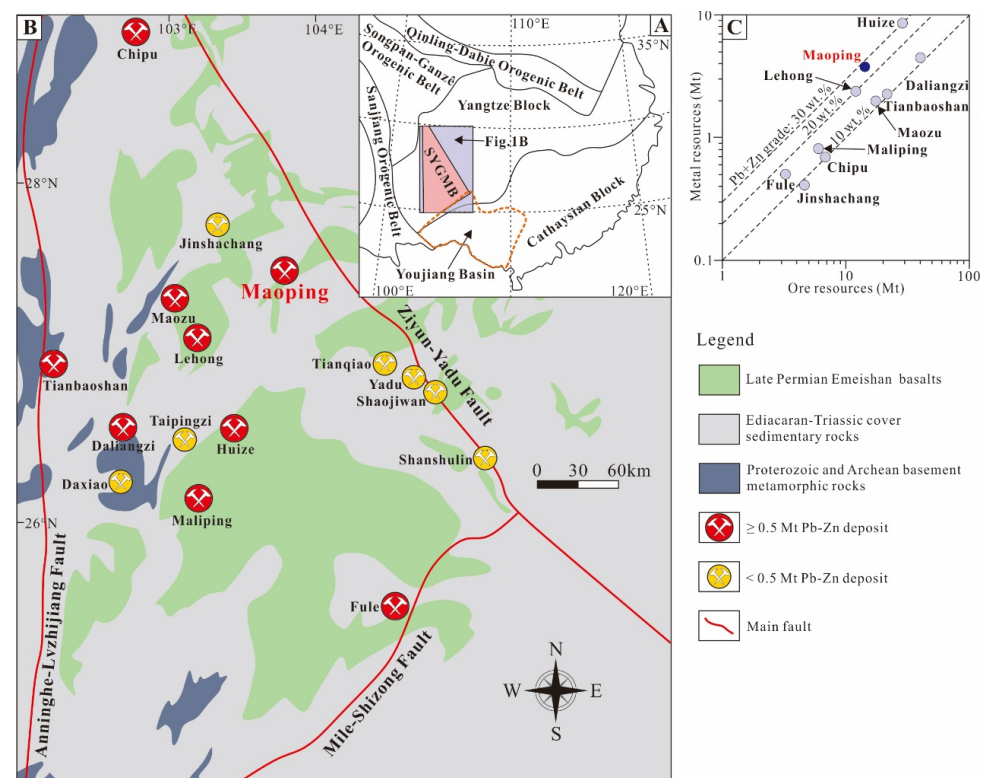


Figure 1. (A) Location of the SYGMB and Youjiang Basin in Southwest China (modified from Luo et al. [38] and Wang et al. [39]). (B) Simplified geological map of the SYGMB, showing Pb–Zn deposits

mentioned in the text (modified from Liu and Lin [15] and Han et al. [21]). (C) Pb + Zn ore resources versus Pb + Zn metal resources, showing some deposits in Figure 2b. Data from Leach and Song [25], Han et al. [29], Luo et al. [38,40], Zhou et al. [41], Ren et al. [42], Li et al. [43], and Zhao et al. [44].

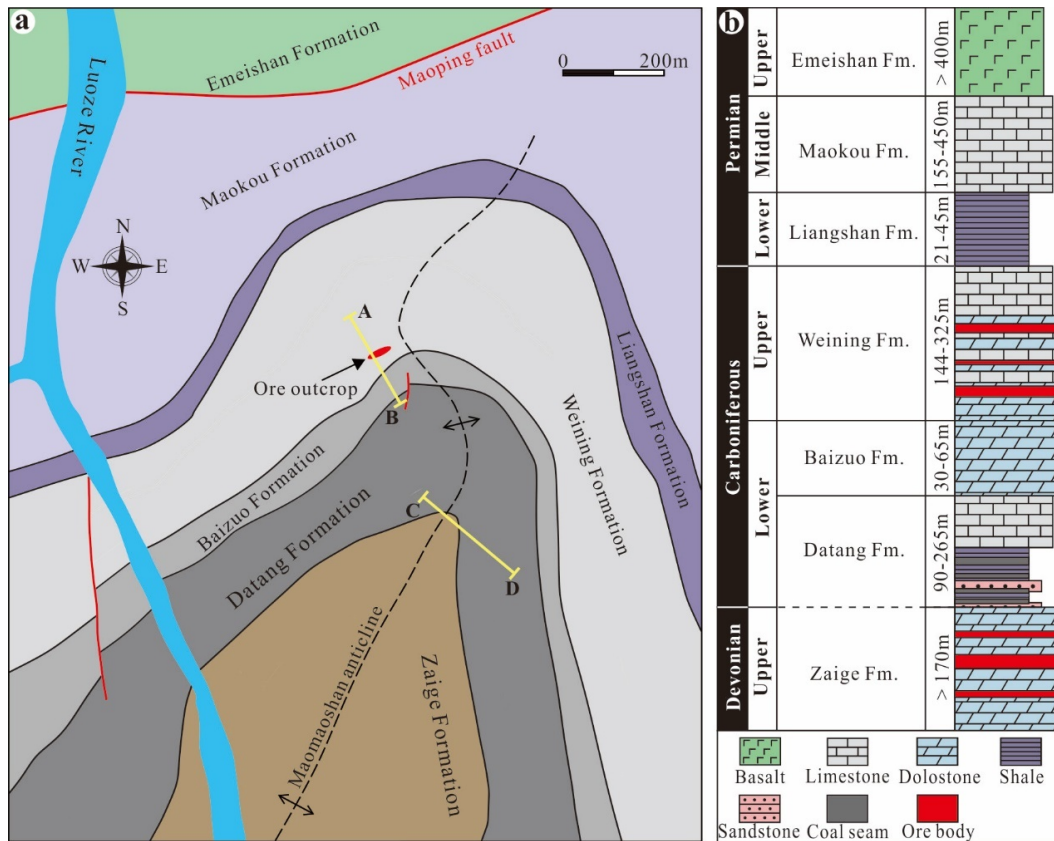


Figure 2. (a) Geological map of the Maoping mining district (modified from Wei et al. [45]). A–B and C–D cross sections are presented in Figure 3. (b) Stratigraphic column of the Maoping mining district, showing lithologies and ore-bearing stratum (modified from Xiang et al. [46]).

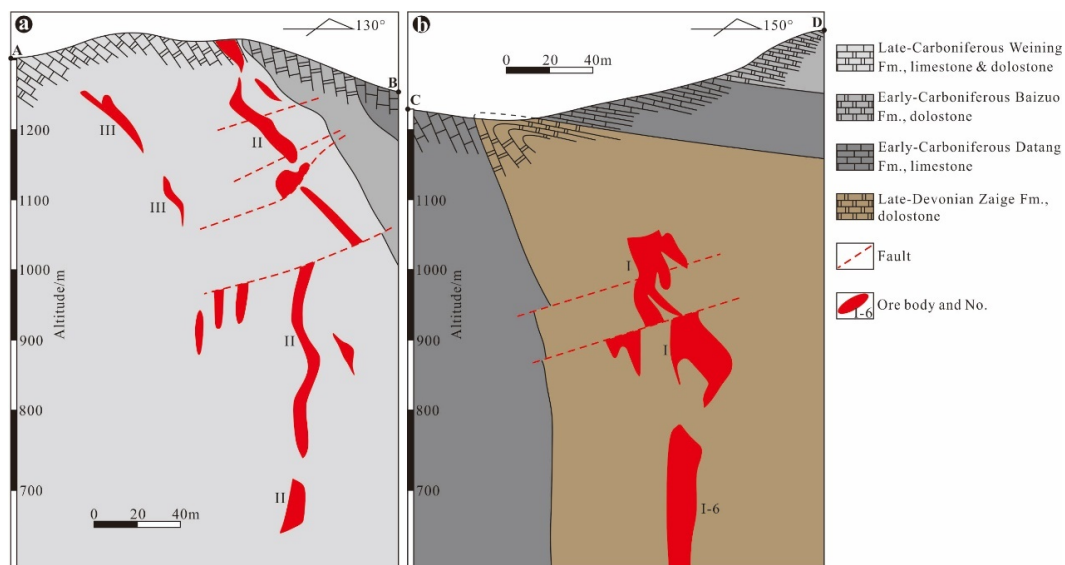


Figure 3. (a) A–B and (b) C–D cross sections, showing the characteristics of ore bodies in the Maoping deposit (modified after Han et al. [47]). The cross-section locations are in Figure 2.

The SYGMB comprises over 400 carbonate-hosted Pb–Zn deposits [15,40,48], which occur in limestone or dolostone of Late Ediacaran to Middle Permian. There are nine known deposits of Pb + Zn metal > 0.5 Mt in the SYGMB, including Huize, Maoping, Lehong, Fule, Maliping, Maozu, Daliangzi, Tianbaoshan, and Chipu (Figure 1B,C).

3. Ore Deposit Geology

3.1. Stratigraphy and Lithology

The strata exposed in the Maoping mining district includes the Upper Devonian Zaige Formation, the Lower Carboniferous Datang and Baizuo Formation, the Upper Carboniferous Weining Formation, the Lower Permian Liangshan Formation, the Middle Permian Maokou Formation, and the Upper Permian Eimeishan Formation (Figure 2a). The Zaige Formation, generally comprising dolostones, is the main ore-bearing strata of the Maoping deposit (Figure 2b). The Datang Formation is subdivided into two members: dark shales interlayered with sandstones and coal seams in the lower member and limestones in the upper member (Figure 2b). The Baizuo Formation is medium-bedded dolostones (Figure 2b). The Weining Formation, generally comprising limestones interbedded with dolostones, is the secondary ore-bearing strata of the Maoping deposit (Figure 2b). The Liangshan and Maokou Formations are shales and limestones, respectively (Figure 2b). The Emeishan Formation is composed of flood basalts (Figure 2b).

3.2. Structure

Structurally, the Maoping fault and Maomaoshan anticline are the main structures of the Maoping mining district (Figure 2a). The Maoping fault, a reverse fault, is approximately 30 km in length and 10–40 m in width, strikes NE trending at 10°–80°, and dips to the SE at an angle of 70°–85° [49]. This fault, which considered the migration pathway of ore-forming fluids [50,51], restricts the location of a series of Pb–Zn deposits with a certain range [47]. The Maomaoshan anticline is a locally overturned anticline, striking NE at a bearing of 20°–45°, and whose NW limb is partially overturned with a dipping angle of 65°–86° and SE limb gently dips an angle of 17°–35° [52]. The known ore bodies of the Maoping deposit occur in the NW wing and plunging end of this anticline.

3.3. Ore Body Characteristics

The Maoping deposit is composed of numerous ore bodies, and almost all ore bodies are concealed. These ore bodies are divided into three main groups (Groups I, II, and III; Figure 3). Group I is hosted in the dolostone of the Late Devonian Zaige Formation, while Groups II and III are hosted within the limestone and dolostone of the Early Carboniferous Weining Formation (Figure 3). They are structurally controlled by bedding fractures [46,50,51] and occur as irregular-thickness veins roughly parallel to stratigraphic bedding (Figure 3). The No. I-6 ore body (Figure 3) is the largest-known ore body, with more than 0.5 Mt of Pb + Zn metal reserves. This ore body's dimensions are 370 m length, 280 m width, and 36.98 m average thickness, containing an average of 7.02 wt.% Pb and 16.93 wt.% Zn [51].

3.4. Mineralogy

The ores are composed of sphalerite, galena, and pyrite as ore minerals, with calcite, dolomite, quartz, and bitumen as gangue minerals (Figures 4 and 5). Massive ores made up of sulfide (sphalerite, galena, and/or pyrite; Figure 4a,b) are predominant, followed by brecciated ores (Figure 4c,d), which consist of sulfide breccias cemented by calcite. Minerals in the ores have replacement (Figure 5a–c), veinlet–vein filling (Figure 5d,e,g), fragmented (Figure 5e), co-dissolved (Figure 5f), euhedral-subhedral granular (Figure 5g), enclosed (Figure 5h), and emulsion (Figure 5i) textures.

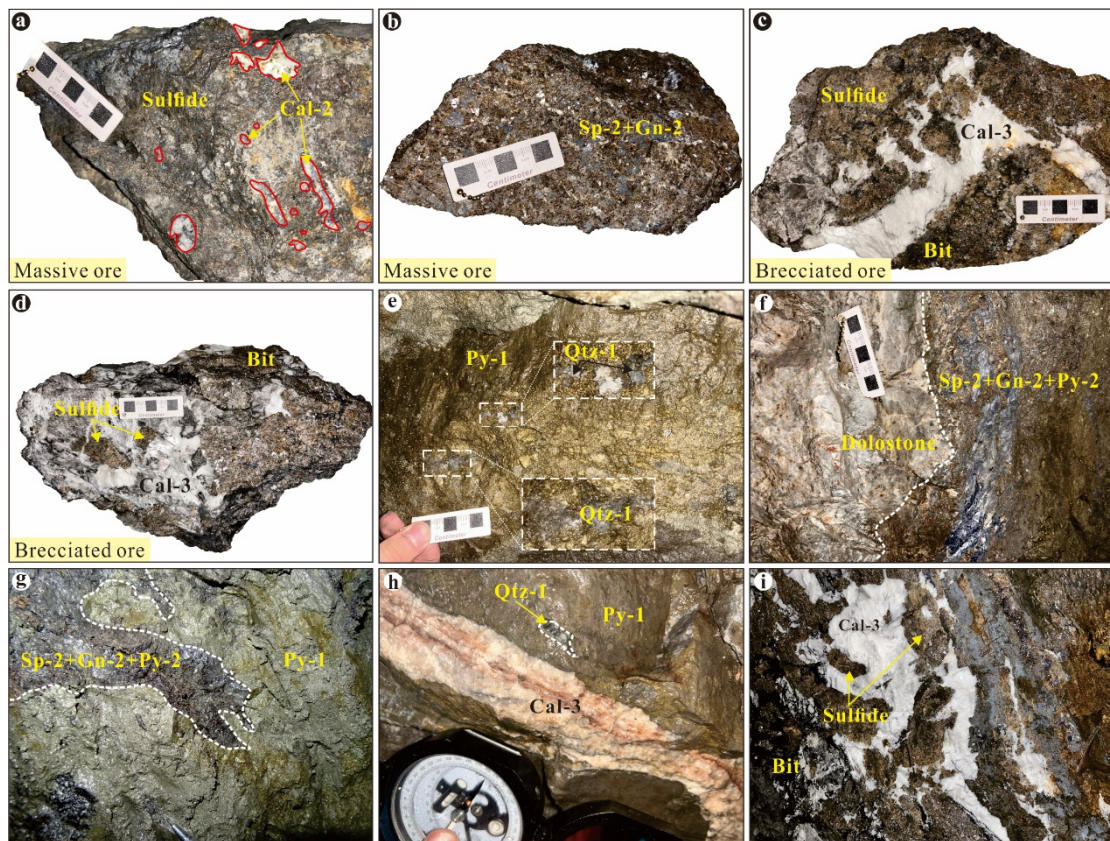


Figure 4. Photographs of field outcrops and hand specimens from the Maoping deposit. (a) Massive ore with an irregular Cal-2 block. (b) Massive ore made up of Sp-2 and Gn-2. (c,d) Brecciated ore made up of sulfide that is cemented by Cal-3. (e) Abundant Py-1 containing minor Qtz-1. (f) Coexisting Sp-2, Gn-2, and Py-2, with a clear boundary with host rock (dolostone). (g) Py-1 invaded by Sp-2+Gn-2+Py-2 veins. (h) Cal-3 vein crosscutting pre-existing Py-1 containing Qtz-1. (i) Sulfide breccias cemented by late Cal-3. Abbreviations: Py = pyrite; Sp = sphalerite; Gn = galena; Cal = calcite; Qtz = quartz; Bit = bitumen.

3.5. Mineral Paragenesis

Based on the mineral assemblages and crosscutting relationships, the hydrothermal period of the Maoping deposit can be subdivided into three stages of mineralization: (I) early ore stage, (II) main ore stage, and (III) late ore stage (Figure 6).

Stage I (pyrite + quartz stage): Abundant pyrites (Py-1) occur in this stage (Figure 4e,g,h). They are characterized by coarse grains (Figure 5a,e). In addition, minor quartz (Qtz-1) can be observed in dense, massive Py-1 (Figure 4e), and sphalerite, galena, and dolomite can be seen occasionally. **Stage II (sphalerite + galena stage):** Major sphalerite and galena (Sp-2 and Gn-2) with minor calcite (Cal-2; Figure 4a) and euhedral-subhedral fine-grained pyrite (Py-2; Figure 5g) are precipitated in this stage, which formed the massive ores (Figure 4f). There are significant crosscutting relationships of mineral assemblages between this stage and Stage I, such as Py-1 invaded by Sp-2 + Gn-2 + Py-2 veins at the macroscopic scale (Figure 4g) and Gn-2 veinlets crosscutting Py-1 at the microscale (Figure 5e). Additionally, quartz and dolomite are rarely seen. **Stage III (calcite stage):** This stage is characterized by the appearance of abundant calcite (Cal-3). It cuts through the mineral assemblages of Stages I and II (Figures 4h and 5g). Notably, early sulfide breccias are frequently cemented by Cal-3, forming brecciated ores (Figure 4i). In this stage, sphalerite, galena, dolomite, and bitumen can be occasionally observed.

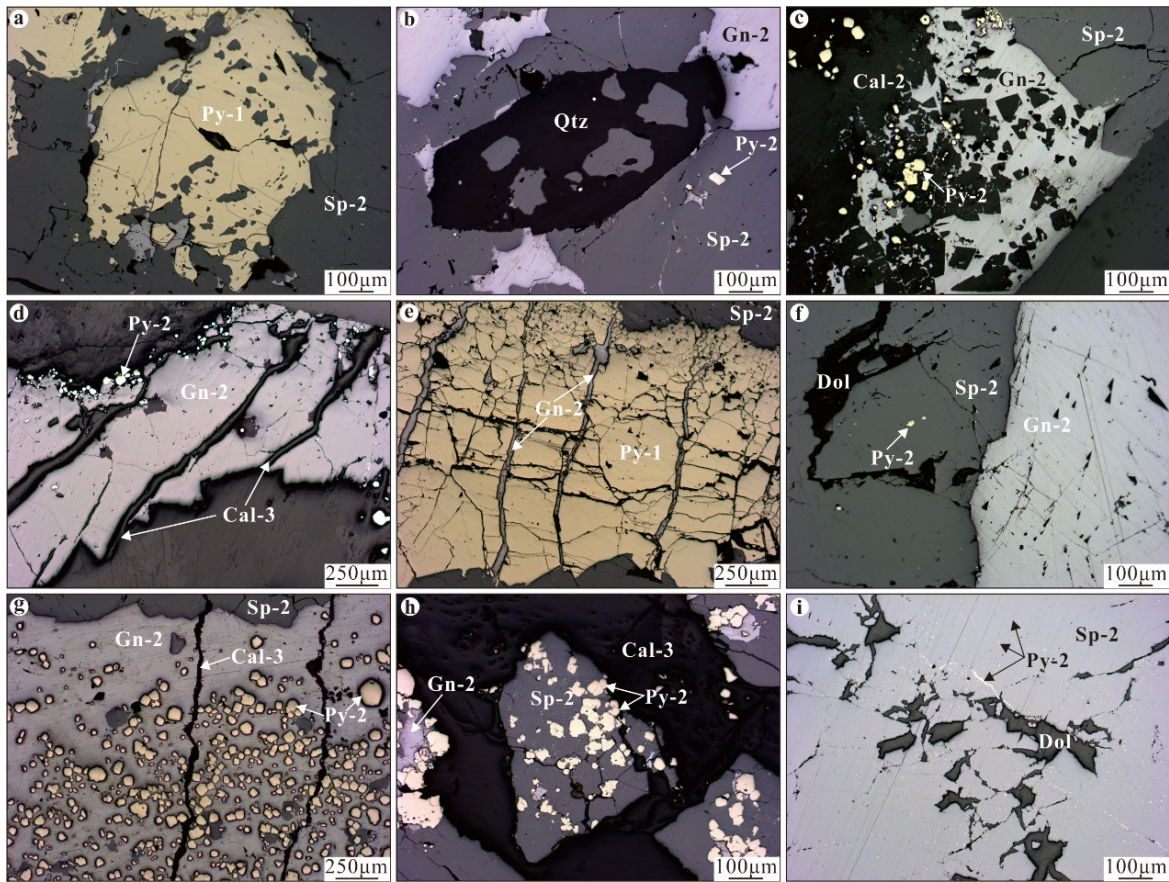


Figure 5. Microphotographs of ore textures observed at the Maoping deposit. (a) Coarse-grained Py-1 replaced by Sp-2. (b) Replacement of hexagonal prism Qtz by Sp-2. (c) Cal-2 replaced by Gn-2. (d) Cal-3 veinlets cutting through pre-existing Gn-2. (e) Late Gn-2 veinlets crosscutting fragmented Py-1. (f) Sp-2 coexisting with Gn-2. (g) Euhedral-subhedral fine-grained Py-2 distributed in Gn-2 and Cal-3 veinlets cutting through pre-existing Gn-2. (h) Sp-2 and Py-2 chips enclosed and cemented by late Cal-3. (i) Inclusions of Py-2 in Sp-2 and Sp-2 fractures filled with Dol. Abbreviations: Py = pyrite; Sp = sphalerite; Gn = galena; Cal = calcite; Qtz = quartz; Dol = dolomite.

Mineral	Hydrothermal period		
	Early ore stage (I)	Main ore stage (II)	Late ore stage (III)
Pyrite	Py-1	Py-2	
Quartz	Qtz-1		
Sphalerite		Sp-2	
Galena		Gn-2	
Calcite		Cal-2	Cal-3
Dolomite			
Bitumen			

Major phase
 Minor phase
 Local phase

Figure 6. Mineral paragenesis of the Maoping deposit.

4. Materials and Methods

4.1. Sampling and Sample Preparation

The sample suite was collected from the underground galleries and drill cores of three main ore body groups (Figure 3). Double-polished thin sections (~200 µm) for fluid-inclusion studies were prepared from the sample suite. Pyrite, calcite, and sphalerite grains (40–80 meshes) were screened from the sample suite for more than 99% purity under a stereomicroscope. Quartz-1, sphalerite-2, calcite-2, and calcite-3 were chosen for fluid-inclusion petrography and microthermometry. One pyrite-2 sample and seven sphalerite-2 samples were selected for cationic compositions of fluid-inclusion extracts. In addition, 10 calcite-2 samples and 17 calcite-3 samples were chosen for H–O isotopic analyses. Five pyrite-1 samples were selected for He–Ar isotopic analyses.

4.2. Analytical Methods

Fluid-inclusion petrography was performed according to Roedder [53] and Lu et al. [54]. Fluid inclusions were classified as primary, pseudosecondary, secondary, or isolated inclusions, with no clear spatial relation to growth zones or fractures (cf. [55]). A Linkam TMS94/1500 heating-freezing system coupled to a Leitz1350 was used for microthermometric measurements at the Institute of Geochemistry, Chinese Academy of Sciences, Guiyang, China. Calibration of the heating and freezing stages was performed by analyzing fluid-inclusion standards before and after each measurement campaign. The range of temperature for the microthermometric measurements was –195 to +600 °C. The estimated accuracy of the freezing and heating measurements was ±0.1 °C for temperatures lower than 25 °C, ±1 °C for temperatures ranging from 25 °C to 300 °C, and ±2 °C for temperatures higher than 300 °C. Salinities were calculated using the final melting temperatures of ice [56].

The extraction of the liquid phase from fluid inclusions was conducted using the thermal explosion method. The explosive conditions of fluid inclusions in pyrite and sphalerite were 700 °C for 10 min and 500 °C for 10 min, respectively. K⁺, Na⁺, Ca²⁺, and Mg²⁺ in the liquid phase were measured using an ion chromatograph (ICS-600) at the Beijing Research Institute of Uranium Geology, Beijing, China (BRIUG). The minimum detection limit was 0.01 mg/L.

Hydrogen and oxygen isotopic analyses were carried out at BRIUG using a MAT-253 mass spectrometer. Fluid inclusions hosted in calcite were thermally decrepitated in vacuum at 550 °C to produce H₂O, which was subsequently reduced to H₂ with a zinc reagent for H isotope study. Oxygen isotopic compositions were analyzed from calcite using the BrF₅ technique. Outcome data were presented as δD and δ¹⁸O values in relation to Vienna Standard Mean Ocean Water (V-SMOW). The analytical precisions were better than ±0.1‰ and ±0.2‰ for δD and δ¹⁸O, respectively.

Helium and argon isotopic analyses were performed using a Helix-SFT noble gas isotope mass spectrometer at BRIUG. Noble gases were extracted from pyrite using a one-step or a multi-step crushing process in a vacuum crusher at 20,000 psi pressure. He and Ar trapped in the cold finger were introduced separately into the mass spectrometer and analyzed in static mode. Line blanks were run before each measurement, producing negligible He blanks (³He < 3 × 10¹⁷ ccSTP) and low Ar blanks (⁴⁰Ar < 4 × 10^{–11} ccSTP), about 0.1% of the signals from samples. Outcome data were calibrated using Helium HESJ standards [57]. Detailed measurement procedures are described by He et al. [58].

5. Results

5.1. Fluid-Inclusion Petrography

Isolated fluid inclusions, with no clear spatial relation to growth zones or fractures, were the empirical criteria for discerning primary fluid inclusions [53,59]. Consequently, isolated inclusions in quartz-1, sphalerite-2, calcite-2, and calcite-3 were interpreted as primary fluid inclusions. In addition, these minerals were also found to contain primary fluid-inclusion assemblages (FIAs) along growth zones, although they also contained

secondary fluid inclusions along healed fractures. Three major types of primary fluid inclusions were observed in these minerals based on the phase present at room temperature: (1) liquid-rich fluid inclusions (LV type) with 5 to 40 vol.% vapor in all minerals (Figure 7), (2) liquid fluid inclusions (L type) in quartz-1 (Figure 7a), and (3) daughter mineral-bearing fluid inclusions (SLV type) in quartz-1 (Figure 7a) and calcite-3 (Figure 7g). Only the LV-type fluid inclusions were analyzed microthermometrically in this study.

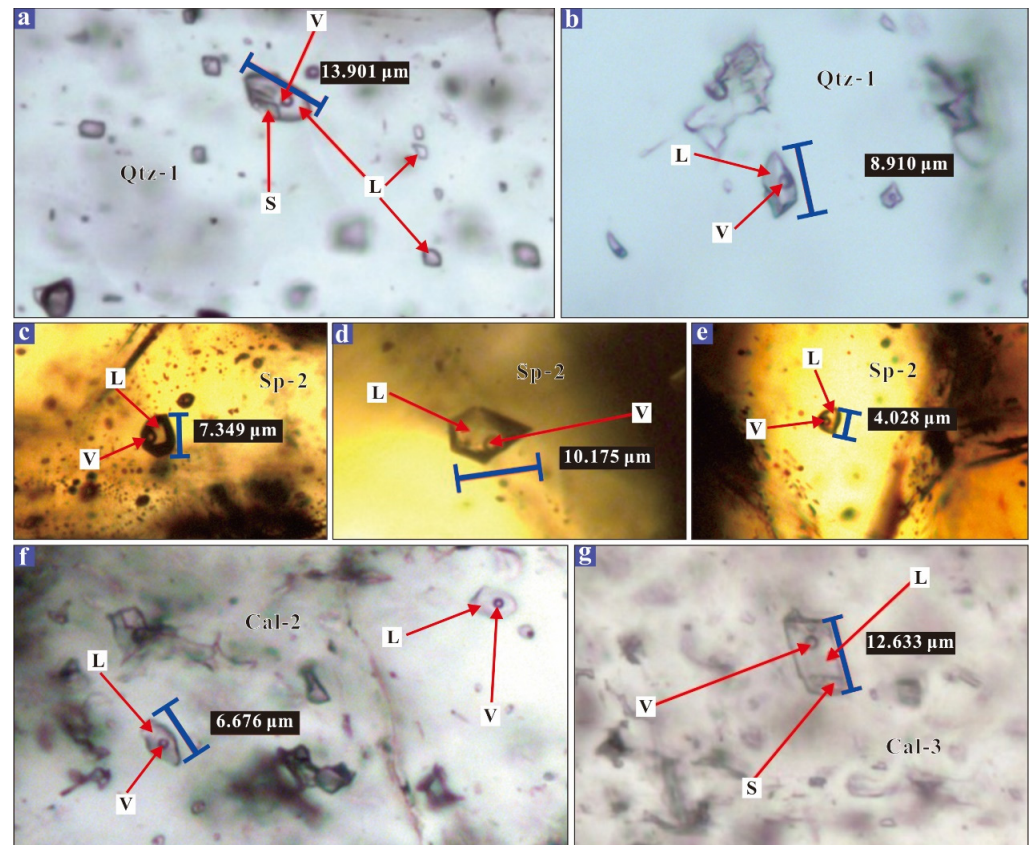


Figure 7. Photomicrographs of primary fluid inclusions from the Maoping deposit samples. (a) SLV- and L-type fluid inclusions in Qtz-1. (b) LV-type fluid inclusions in Qtz-1. (c–e) LV-type fluid inclusions in Sp-2. (f) LV-type fluid inclusions in Cal-2. (g) SLV-type fluid inclusion in Cal-3. Abbreviations: L = liquid; V = vapor; S = solid; Qtz = quartz; Sp = sphalerite; Cal = calcite.

5.2. Microthermometry

Microthermometric data collected from the different stages are summarized in Table 1. The complete dataset is included in Supplementary Table S1. The fluid inclusions in quartz-1 showed homogenization temperatures (T_h) ranging from 290 to 390 °C, with the majority falling between 300 and 340 °C (Figure 8a), and had salinities varying between 0.2 and 7.6 wt.% NaCl eqv., with the majority falling between 2 and 6 wt.% NaCl eqv. (Figure 8b). The fluid inclusions in sphalerite-2 had a T_h of 217 to 314 °C, with a peak range of 240 to 300 °C (Figure 8a), and salinities of 3.9 to 14.1 wt.% NaCl eqv., with a peak range of 6 to 10 wt.% NaCl eqv. (Figure 8b). The fluid inclusions in calcite-2 had a T_h of 217 to 278 °C, with a peak range of 220 to 260 °C (Figure 8a), and salinities of 5.3 to 13.4 wt.% NaCl eqv., with a peak range of 6 to 10 wt.% NaCl eqv. (Figure 8b). The T_h and salinities of the fluid inclusions in calcite-3 ranged from 135 to 214 °C (160 to 200 °C peak value; Figure 8a) and 8.9 to 21.3 wt.% NaCl eqv. (12 to 16 wt.% NaCl eqv. peak value; Figure 8b), respectively.

Table 1. Summary of microthermometric data on fluid inclusions from the Maoping deposit.

Stage	Host	N	T _m (°C)		T _h (°C)		Salinity (wt.% NaCl Eqv.)	
			Range	Mean	Range	Mean	Range	Mean
I	Quartz	34	−4.8 to −0.1	−2.3	290 to 390	329	0.2 to 7.6	3.8
II	Sphalerite	21	−10.2 to −2.3	−5.7	217 to 314	268	3.9 to 14.1	8.7
II	Calcite	19	−9.5 to −3.2	−6.4	217 to 278	241	5.3 to 13.4	9.6
III	Calcite	35	−18.4 to 5.8	−10.7	135 to 214	178	8.9 to 21.3	14.5

Note: Salinity = 0.00 + (1.78 × A) − (0.0442 × A²) + (0.000557 × A³), where A is the absolute value of the last ice-melting temperature (T_m) [56].

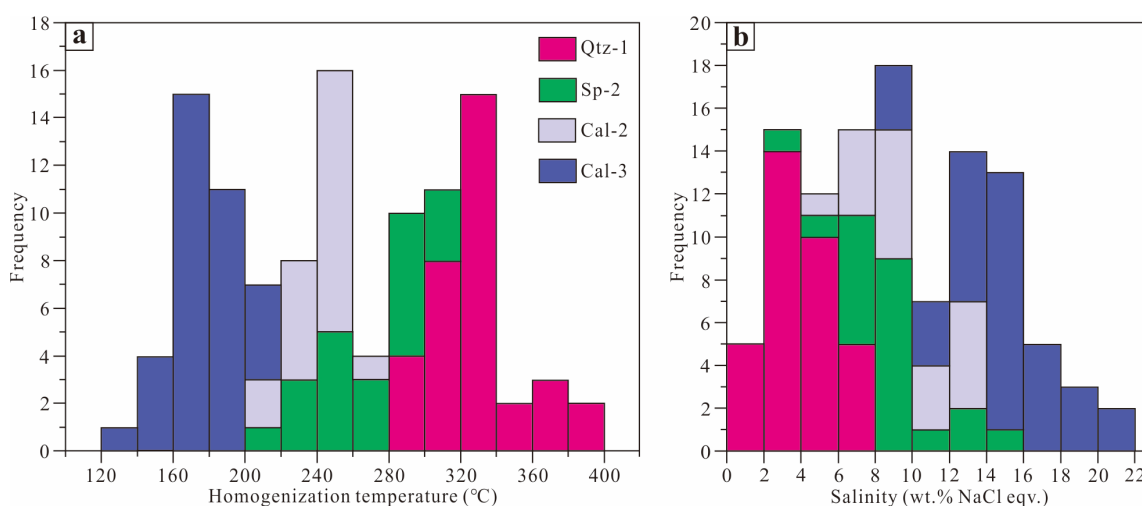


Figure 8. Stacked histograms of the homogenization temperatures (a) and salinities (b) of fluid inclusions in the Maoping deposit. Abbreviations: Qtz = quartz; Sp = sphalerite; Cal = calcite.

5.3. H–O Isotopic Compositions

Hydrogen and oxygen isotopic compositions obtained from calcite of Stages II and III are presented in Table 2. The δD_{V-SMOW} and δ¹⁸O_{H₂O} values of calcite from Stage II ranged from −71.4 to −50.0‰ (mean −65.1‰) and +11.4 to +13.7‰ (mean +12.2‰), respectively, while those of calcite from Stage III varied from −78.7 to −50.3‰ (mean −66.4‰) and +7.4 to +9.9‰ (mean +8.5‰), respectively.

Table 2. Compositions of hydrogen and oxygen isotopes in calcite from the Maoping deposit.

Sample No.	Stage	Mineral	δD _{V-SMOW} /‰	δ ¹⁸ O _{V-SMOW} /‰	T/°C	δ ¹⁸ O _{H₂O} /‰
KGR02		Calcite	−50.0	21.3	241	13.7
KHr-13		Calcite	−58.9	19.0	241	11.4
KGr-11-1		Calcite	−66.4	19.4	241	11.8
KHr-21-1		Calcite	−70.8	21.0	241	13.4
KHr-21-3	II	Calcite	−67.9	19.2	241	11.6
KHr-21-4		Calcite	−71.9	19.7	241	12.1
KHr-23		Calcite	−59.6	19.5	241	11.9
KZr-11		Calcite	−63.9	19.3	241	11.7
KZr-13		Calcite	−74.1	20.1	241	12.5
KPr-11-2		Calcite	−67.0	19.6	241	12.0

Table 2. Cont.

Sample No.	Stage	Mineral	$\delta D_{V-SMOW}/\text{‰}$	$\delta^{18}O_{V-SMOW}/\text{‰}$	T/°C	$\delta^{18}O_{H_2O}/\text{‰}$
KHr5-2		Calcite	−64.3	19.0	178	8.2
KHr5-3		Calcite	−72.6	19.0	178	8.2
KPr-2		Calcite	−69.3	19.2	178	8.4
KPr-504-3		Calcite	−78.7	19.1	178	8.3
KLR6-3		Calcite	−73.8	19.0	178	8.2
KLR-7		Calcite	−74.8	19.2	178	8.4
KHr-11		Calcite	−70.3	18.9	178	8.1
KHr-12		Calcite	−77.3	18.2	178	7.4
KZr-12	III	Calcite	−70.7	19.1	178	8.3
KZr-13-1		Calcite	−56.5	19.3	178	8.5
KGR-66-1		Calcite	−60.8	20.7	178	9.9
KGR-72-2		Calcite	−61.9	20.6	178	9.8
KG-303		Calcite	−61.3	18.4	178	7.6
KPr-601		Calcite	−68.4	19.4	178	8.6
KZ-HX-1r		Calcite	−52.1	18.2	178	7.4
KZ-HX-2r		Calcite	−65.8	19.9	178	9.1
HX-850		Calcite	−50.3	19.9	178	9.1

Note: $1000 \ln \alpha_{(\text{calcite-H}_2\text{O})} = 2.78 \times 10^6 / (T + 273.15)^2 - 2.89$ [60]; temperature (T) is based on the mean value of homogenization temperatures yielded by fluid inclusions in calcite from the Maoping deposit (Table 1).

5.4. He–Ar Isotopic Compositions

The analytical results of He and Ar isotopic compositions of fluid inclusions hosted in pyrite from the Maoping deposit are exhibited in Table 3. The ^4He concentrations ranged from 1.33×10^{-7} to 10.4×10^{-7} ccSTP/g, and the $^3\text{He}/^4\text{He}$ ratios were between 0.05 and 0.08 Ra, where Ra is the $^3\text{He}/^4\text{He}$ ratio of air, with a value of 1.40×10^{-6} [61]. The ^{40}Ar concentrations ranged from 4.12×10^{-7} to 26.8×10^{-7} ccSTP/g, with $^{40}\text{Ar}/^{36}\text{Ar}$ ratios of 309.7 to 746.9. The $^{40}\text{Ar}^*$ was radiogenic ^{40}Ar , and the $^{40}\text{Ar}^*/^4\text{He}$ ratios were between 0.53 and 0.96, using the formula $^{40}\text{Ar}^*/^4\text{He} = (^{40}\text{Ar} - 295.5 \times ^{36}\text{Ar})/^4\text{He}$ [62]. Pyrite samples in this study were collected underground, so cosmogenic He was not considered a source of ^3He [63–65]. The $F^4\text{He}$ values, defined as the $^4\text{He}/^{36}\text{Ar}$ ratios of samples compared to those of the atmosphere (0.1655; [66]), ranged from 181 to 4797, indicating that the volatiles released from the pyrite samples contain negligible atmospheric He (cf. [66]). Consequently, the He and Ar isotopic compositions of fluid inclusions in these samples can represent those of ore-forming fluid.

Table 3. Helium and argon isotopic compositions of fluid inclusions in pyrite from the Maoping deposit.

Sample No.	Host	^4He (10^{-7})	$^3\text{He}/^4\text{He}$ (Ra)	^{40}Ar (10^{-7})	$^{40}\text{Ar}^*/^4\text{He}$	$^{40}\text{Ar}/^{36}\text{Ar}$	$F^4\text{He}$
KHr5-6	Pyrite-1	7.23	0.05	11.4	0.58	467.6	1790
KHr6	Pyrite-1	10.4	0.05	9.80	0.57	746.9	4797
KHr8-1	Pyrite-1	7.50	0.05	10.1	0.53	486.8	2189
KHr8-2	Pyrite-1	2.59	0.07	26.8	0.48	309.7	181
KHr43-3	Pyrite-1	1.33	0.08	4.12	0.96	427.7	837

Note: The unit for ^4He and ^{40}Ar is ccSTP/g; Ra is the $^3\text{He}/^4\text{He}$ ratio of air (1.4×10^{-6}).

6. Discussion

6.1. Reliability of Fluid-Inclusion Data

There is an assumption in fluid-inclusion studies that the integrity of fluid inclusions since their time of formation has been preserved [53]. Fluid-inclusion re-equilibration toward greater volumes (lower densities) caused by plastic deformations or the partial leakage of fluid inclusions caused by overheating can result in anomalously high T_h values and an overestimate of ore-forming temperatures [67]. The fluid-inclusion microthermome-

try of some deposits (e.g., Huize) in the SYGMB exhibit widely variable and abnormally high T_h (data concentrated 150 to 221 °C and 320 to 364 °C [68,69]) for an MVT deposit, which has been questioned by some authors. Here, it is necessary to estimate the reliability of fluid-inclusion data for the Maoping deposit, although no post-mineralization plastic deformations have been observed in this deposit.

The potential for fluid inclusions' re-equilibration during overheating largely depends on the fluid inclusions' size and host mineral strength [70,71]. Consequently, the plot of fluid-inclusion size (maximum dimension) against T_h has been used to evaluate whether fluid inclusions were re-equilibrated [67,72]. A positive correlation should be displayed in this plot if re-equilibration has occurred, and this effect would be significant for softer minerals (e.g., calcite) [67]. For all datasets, there was no positive correlation in any host minerals (Figure 9). In addition, quartz had the highest T_h values, followed by sphalerite and then calcite, which is opposite to the higher T_h of softer minerals after re-equilibration. The last evidence for preservation of fluid-inclusion integrity is that fluid inclusion in the same minerals typically showed a relatively narrow range of T_h values that was much less than that between different minerals (Figure 9). Certainly, this would also be interpreted as different precipitation temperatures of these minerals.

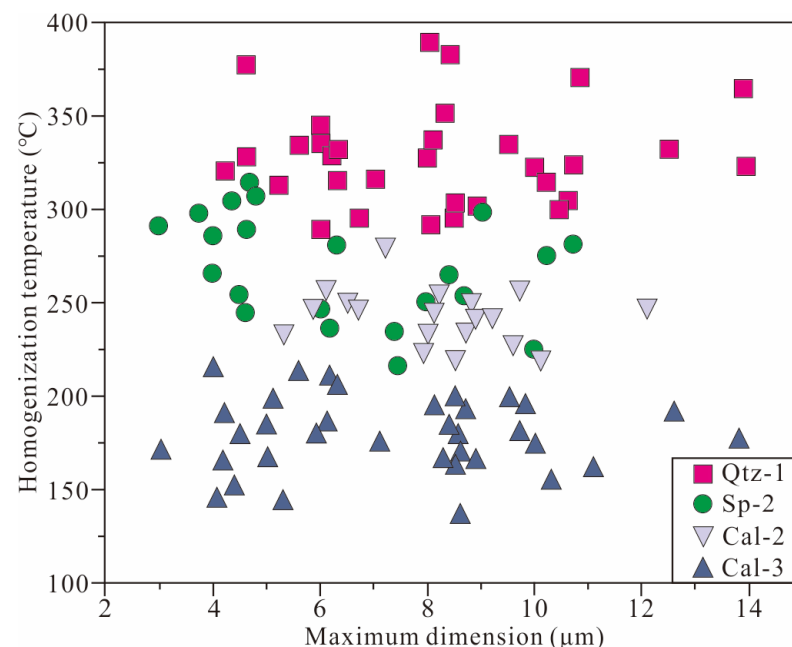


Figure 9. Plot of homogenization temperatures as a function of maximum inclusion dimensions for the Maoping deposit. Abbreviations: Qtz = quartz; Sp = sphalerite; Cal = calcite.

6.2. Definition for Two Types of Fluids

Fluid inclusions in minerals from the Maoping deposit showed a large variation in temperatures (135 to 390 °C; Figure 8a) and salinities (0.2 to 21.3 wt.% NaCl eqv.; Figure 8b). This variation can be commonly explained by the mixing of multiple fluids during ore deposition [67,73]. In addition, there are three groups of fluid inclusions with distinct T_h and salinities in the Maoping deposit (Figure 10a). The Stage I group has the characteristics of metamorphic fluids in temperature and salinity. Most of the Stage III group falls into the basal brine field. The Stage II group is between Stage I and Stage III, which seems to indicate the mixing of metamorphic fluids and basal brines.

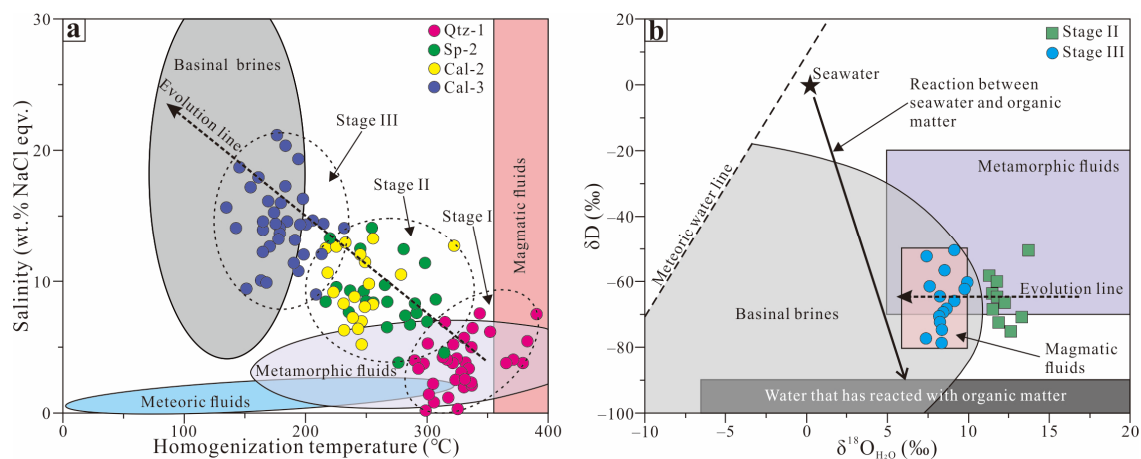


Figure 10. (a) Plot of homogenization temperatures and salinities of fluid inclusions in different ore stages of the Maoping deposit (base map from Kesler [1]). Abbreviations: Qtz = quartz; Sp = sphalerite; Cal = calcite. (b) Plot of δD versus $\delta^{18}O_{H_2O}$ for calcite in the Maoping deposit (base map from Taylor [74]). The field of basinal brines is from Kesler [1].

The fluid δD (obtained by direct measurement of fluid inclusions) and fluid $\delta^{18}O$ values (based on mineral compositions and mineral–water fractionation factors) from hydrothermal period samples were widely used to trace the fluid sources [59,75–79]. The $\delta^{18}O_{H_2O}$ values of fluids for Stage II (+11.4 to +13.7‰; Table 3) were significantly higher than those of magmatic fluids (+7 to +9‰; [74]) and were similar to those of metamorphic fluids (+5 to +25‰; [74]). The $\delta^{18}O_{H_2O}$ values of fluids for Stage III ranged from +7.4 to +9.9‰ (Table 2), which overlap those of magmatic fluids. Nevertheless, Stage III fluids with low temperature and high salinity are more likely to be basinal brines (Figure 10a). In the δD versus $\delta^{18}O_{H_2O}$ plot (Figure 10b), moreover, the H–O isotopic data of fluids for Stages III can all fall into the basinal brine field identified by Kesler [1], while those of fluids for Stages II fall between the metamorphic fluid field and the basinal brine field (Figure 10b), which can be explained by a mixing of these two fluids.

Although fluids for Stage I are characterized by metamorphic fluids (Figure 10a), their high temperatures can also be suspected to be due to mantle fluids (or magmatic fluids), especially in the case of the presence of EFBs in SYGMB (Figure 1B). The EFBs (c. 260 Ma [37]) are spatially associated with Pb–Zn deposits in the SYGMB but are much older than these deposits (194–230 Ma; see [21] and references therein). However, stable isotope studies suggest that magmatic fluids originating from EFBs should be partly responsible for these deposits ([18] and references therein).

Isotopic compositions of noble gases in paleofluids are being intensively used to track the sources of volatiles and heat in ore-forming fluids [61,80–83]. Pyrite is a suitable noble gas carrier due to the negligible He and Ar diffusion coefficients of its fluid inclusions [62]. Here, pyrite from Stage I was used to analyze the He–Ar isotopic compositions to reflect the origin of high-temperature fluids for Stage I. In the 4He versus 3He plot (Figure 11a), the $^3He/^4He$ ratios (0.05–0.08 Ra) were slightly higher compared to crust lines (0.01–0.05 Ra) and notably lower compared to the mantle line (6–9 Ra), indicating that the high-temperature fluids are dominated by crust fluids. The He_{mantle} (%) values (proportion of mantle-derived He) varied between 0.67% and 1.17%, as calculated by the formula [66] $He_{mantle}(\%) = [(^3He/^4He)_{sample} - (^3He/^4He)_{crust}] / [(^3He/^4He)_{mantle} - (^3He/^4He)_{crust}]$, where $(^3He/^4He)_{mantle} = 0.01$ Ra, $(^3He/^4He)_{crust} = 6.00$ Ra, and $(^3He/^4He)_{sample} = 0.05 - 0.08$ Ra. These values indicate a negligible proportion of mantle-derived He in the high-temperature fluids. In the plot of $^{40}Ar/^{36}Ar$ versus $^3He/^4He$ (Figure 11b), similarly, the data points suggest a negligible mantle source component.

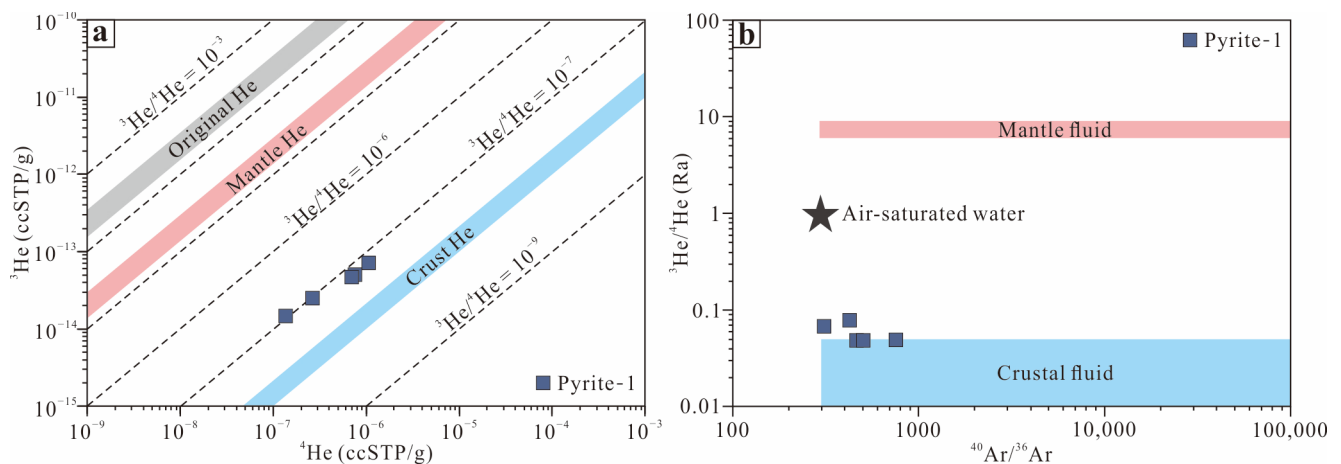


Figure 11. Plots of (a) ^4He versus ^3He and (b) $^{40}\text{Ar}/^{36}\text{Ar}$ versus $^3\text{He}/^4\text{He}$ for fluid inclusions in pyrite from the Maoping deposit (base map from Mamyin and Tolstikjin [84]).

6.3. A Genetic Model for the Maoping Deposit

The continental basin and its distal parts are a common tectonic setting for carbonate-hosted Pb–Zn deposits [11,13,25,67]. The Youjiang foreland basin, located along the SE border of the SYGMB (Figure 1A), was uplifted into a fold belt during the Late Triassic to Early Jurassic [39,85,86]. The Pb–Zn mineralization ages for the SYGMB (such as c. 203 Ma yielded by Maoping sphalerite Rb–Sr isotope geochronology [48]) coincide with the well-constrained episode of the evolution of the Youjiang foreland basin, suggesting basinal brines originating from the basin are related to the mineralization [24,48,87].

High maturation values are observed in the Youjiang Basin, where the vitrinite reflectance values ($R_m > 3\%–4\%$ [88,89]) and conodont alteration indices (CAI > 3–5 [90]) imply paleogeotemperatures of 200–350 °C during the Late Permian to Middle Triassic. Given the thermal anomaly, medium- to high-temperature basinal brines are considered to contribute to Pb–Zn mineralization in the SYGMB [48,86]. The contradiction between moderate- to high-temperature basinal brines identified by paleogeotemperatures and low-temperature basinal brines identified by fluid-inclusion data is problematic. The basinal brines with long-distance migration (>400 km from the thermal center of the Youjiang Basin to the Maoping deposit) will result in the temperature falling significantly due to the water–rock reaction. Furthermore, the paleogeothermal value does not seem to reflect the true temperature of fluids, especially in the Irish Midlands basin, where the R_m and CAI values indicate abnormal temperatures (300 to 550 °C) that are difficult to compare with fluid-inclusion data (100 to 250 °C) [67,91,92]. Lastly, the R_m and CAI values recorded in the Upper Permian and Middle Triassic series of the Youjiang Basin are also likely due to magmatic hydrothermal overprinting during the Early Cretaceous, with extensive magmatic activity [39,93]. Consequently, low-temperature basinal brines originating from the Youjiang Basin are more likely to contribute to the Maoping deposit, considering the aforementioned points. However, the basement containing a series of low- to high-grade metamorphic rocks [33,34] is a potential source of high-temperature metamorphic fluids, which is supported by isotopic evidence. The tracing of Pb–Zn–Cd–Sr isotopes indicates that the basement is an important source of ore-forming materials in the Maoping deposit [46,48,94].

Based on these findings, a possible genetic model for Maoping was proposed in Figure 12. During the Late Triassic to Early Jurassic, a large number of thrust fold belts, including the Youjiang fold belt and the Maoping thrust fold belt (Maomaoshan anticline and Maoping fault; Figure 2a), occurred in the southwestern part of the Yangtze Block due to intense tectonic compression (Indosinian Orogeny) [21,95–97]. Because the Youjiang foreland basin was uplifted over the Youjiang fold belt, basinal brines originating from the Youjiang Basin migrated to the northwest (Sichuan–Yunnan–Guizhou region) as a result

of gravity and/or tectonic dynamics [24,48]. During the basinal brines' migration, Pb and Zn were extracted from cover sedimentary rocks and SO_4^{2-} was obtained from the sulfate evaporate (gypsum) layers distributed not far from the Maoping mining district [98]. Afterward, coalbed methane (CH_4) in the Carboniferous coal seam (Figure 2b) of the Maoping mining district acted as a reducing agent and transformed the SO_4^{2-} in the basinal brine into H_2S through thermochemical sulfate reduction (TSR). However, the metamorphic fluids extracting Pb and Zn from basement metamorphic rocks migrated upward along the Maoping fault, which was a response to tectonic compression. These rising fluids were more buoyant due to their higher temperatures and lower salinities and were consequently able to punch through cover sedimentary rocks to reach the mineralization site. Finally, the low-temperature and medium-high salinity basinal brines and high-temperature and low-salinity metamorphic fluids were mixed in the bedding fractures of the sedimentary rock cover and mineralization occurred. In the early ore stage (Stage I), metamorphic fluids were predominant in the mixed fluids, showing high temperature and low salinity. With the evolution of mixed fluids, the proportion of basinal brines was higher in the late ore stage (Stage III), and the mixed fluids had the characteristics of low temperature and high salinity.

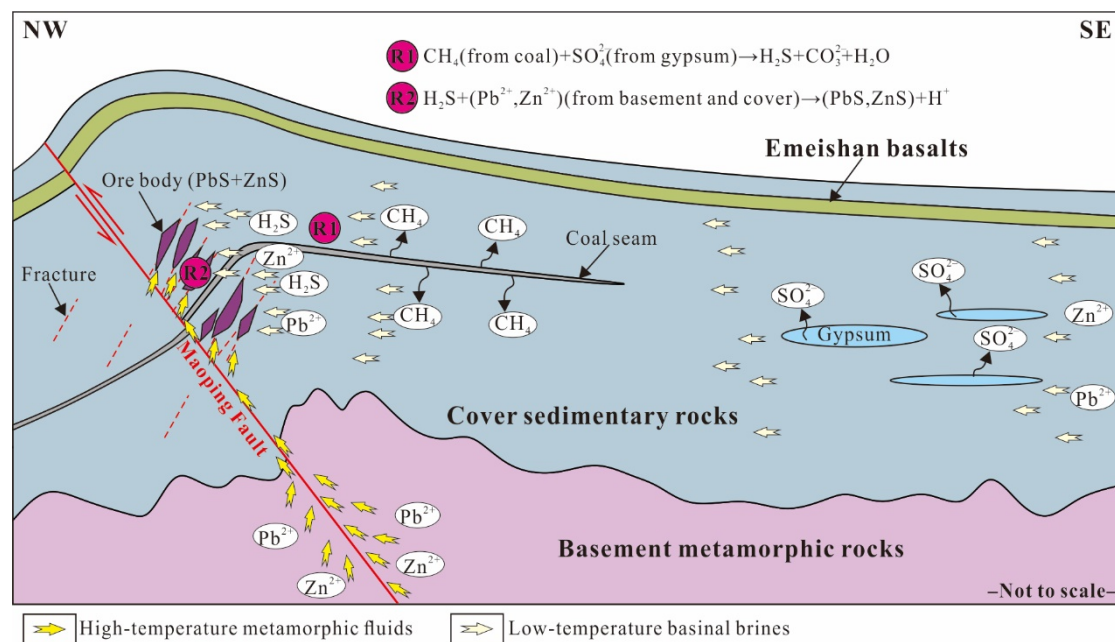


Figure 12. Fluid-mixing model for the Maoping deposit.

6.4. Implications for Carbonate-Hosted Deposits in the SYGMB

In terms of T_h –salinity properties (Figure 13A), the fluids associated with MVT deposits (temperatures of 50 to 200 °C and salinities of 10 to 30 wt.% NaCl eqv. [13]) do not clearly fit the regional pattern in the SYGMB (temperatures of 100 to 400 °C and salinities of 0 to 20 wt.% NaCl eqv.; Figure 13A). In the δD – $\delta^{18}\text{O}$ diagram (Figure 13B), furthermore, the SYGMB Pb–Zn metallogenic hydrothermal system shares much of the complexity. Although the H–O isotopes of fluids in the most deposits are either in the field of the Youjiang Basin brines or in the field of metamorphic fluids, those in the Jinshachang and Chipu deposits fall more into the field of organic water. It is noteworthy that plotting the principal modal T_h and salinity data from the SYGMB (Figure 13A) shows that the high-grade Pb–Zn deposits (e.g., Huize, Maoping, and Lehong with an average grade of $\text{Pb} + \text{Zn} \geq 20$ wt.%; Figure 1C) are characterized by a wide range of T_h and salinities.

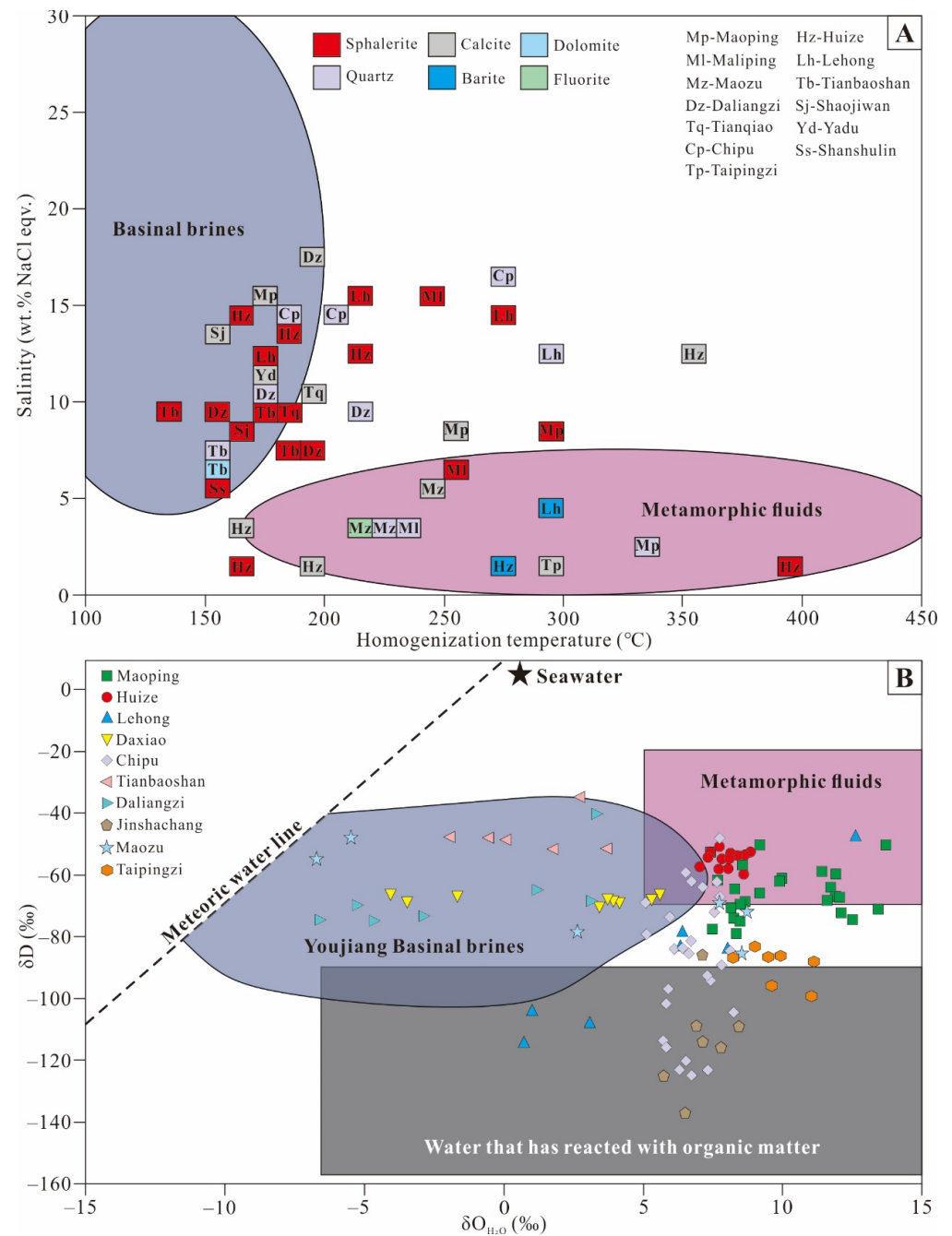


Figure 13. (A) Modal homogenization temperature–salinity plot for carbonate-hosted Pb–Zn deposits in the SYGMB (base map from Kesler [1]). Data from Han et al. [20,68], Luo et al. [38], Wang et al. [69], Zhang et al. [99], Zhao et al. [100], Wang [101], Yang [102], Wang et al. [103], and Ding et al. [104]. See Supplementary Table S2 for details. (B) δD versus $\delta^{18}O_{H_2O}$ plot for minerals from carbonate-hosted Pb–Zn deposits in the SYGMB (base map and field of Youjiang basinal brines from Taylor [74] and Wang et al. [105], respectively). Data from Zhou et al. [41], Zhao et al. [44], Liu et al. [97], Wang et al. [103], Ding et al. [104], Li et al. [106], Wu et al. [107], Yuan et al. [108], and Yang et al. [109]. See Supplementary Table S3 for details.

Such high-grade deposits require the fluids to carry abundant metals for ore deposition. There are three commonly proposed depositional processes in carbonate-hosted Pb–Zn deposits: (1) The reduced sulfur model is identified as reduced sulfur and metals to be transported together to the mineralization site [110,111], (2) the local sulfate reduction model calls upon migrating sulfate and metals to the mineralization site, where CH_4 or

other organic matter reduces sulfate and precipitates Pb–Zn sulfide [112,113], and (3) the mixing model is described as the mixing of metal-rich fluids with H₂S-rich fluids at the depositional site [114,115].

The effect of the activity of reduced sulfur is considered the most important factor that controls the solubility of Pb and Zn in the fluids [116]. The occurrence of reduced sulfur in the fluids limits the base metal concentrations in the fluids to only a few ppm [73]. Thus, the reduced sulfur model is not suitable for high-grade deposits. It is proposed that the combination of models 1 and 2 is a possible mechanism of ore deposition for some high-grade deposits in the SYGMB. We can describe it as the mixing of metal-rich but reduced sulfur-poor metamorphic fluids with basinal brines rich in metals and sulfate at the depositional site, where organic matter (e.g., CH₄) reduces sulfate and precipitates sulfide. This model requires that the basinal brines carry a large amount of sulfate to provide enough reduced sulfur to precipitate to abundant Pb–Zn sulfide. The SYGMB high-grade deposits where organic matter appears can be explained by this model.

7. Conclusions

Three mineralization stages are recognized in the Maoping deposit based on the mineral assemblages and crosscutting vein relationships, i.e., (I) the pyrite + quartz stage, (II) the sphalerite + galena stage, and (III) the calcite stage. Stage I forms in high-temperature (300 to 340 °C) and low-salinity (2 to 6 wt.% NaCl eqv.) fluids. Moderate-temperature (220 to 260 °C) and moderate-salinity (6 to 10 wt.% NaCl eqv.) fluids are observed in Stage II. Fluids in Stage III are characterized by low temperature (160 to 200 °C) and high salinity (12 to 16 wt.% NaCl eqv.).

Metamorphic fluids and basinal brines are identified by fluid-inclusion measurements, together with hydrogen and oxygen isotope data. Helium and argon isotope data show a negligible mantle source component, suggesting magmatic fluids derived from Permian Emeishan basalts have no contribution to ore-forming fluids. The high-temperature and low-salinity metamorphic fluids originating from the Precambrian basement mixed with the low-temperature and high-salinity basinal brines in the Maoping district, and Pb–Zn mineralization occurred.

Regional-scale data show large-scale heterogeneity in fluid properties, including basinal brines, metamorphic fluids, and organic fluids. A possible precipitation model for high-grade Pb–Zn deposits in the SYGMB is described as the mixing of metal-rich but reduced sulfur-poor metamorphic fluids with basinal brines rich in metals and sulfate at the depositional site, where organic matter reduces sulfate and precipitates sulfide.

Supplementary Materials: The following supporting information can be downloaded at <https://www.mdpi.com/article/10.3390/min13050600/s1>: Table S1: Complete dataset for microthermometry on fluid inclusions from the Maoping deposit. Table S2: Microthermometric data on fluid inclusions for carbonate-hosted Pb–Zn deposits in the SYGMB. Table S3: Hydrogen and oxygen isotope data for carbonate-hosted Pb–Zn deposits in the SYGMB.

Author Contributions: Conceptualization, L.W. and R.H.; methodology, L.W. and X.L.; software, L.W.; validation, R.H. and Y.Z.; formal analysis, L.W. and Y.Z.; investigation, L.W., R.H., Y.Z. and X.L.; resources, R.H. and Y.Z.; data curation, L.W. and X.L.; writing—original draft preparation, L.W.; writing—review and editing, R.H. and Y.Z.; visualization, L.W.; supervision, R.H. and Y.Z.; project administration, R.H. and Y.Z.; funding acquisition, R.H. and Y.Z. All authors have read and agreed to the published version of the manuscript.

Funding: This work was jointly supported by the National Natural Science Foundation of China (grant nos. 41802089, 42172086, 41572060, and U1133602), the China Postdoctoral Science Foundation (grant no. 2017M610614), the Yunnan Major Scientific and Technological Projects (grant no. 202202AG050014), the Ten Thousand Talent Program of Yunnan Province (grant no. YNWR-QNBJ-2019-157), the Projects of the YM Lab (2011), and the Innovation Team of the Yunnan Province (2008 and 2012).

Data Availability Statement: All data are contained within the article and Supplementary Materials.

Conflicts of Interest: The authors declare no conflict of interest.

References

1. Kesler, S.E. Ore-forming fluids. *Elements* **2005**, *1*, 13–18. [[CrossRef](#)]
2. Yardley, B.W.D. Metal concentrations in crustal fluids and their relationship to ore formation. *Econ. Geol.* **2005**, *100*, 613–632. [[CrossRef](#)]
3. Liebscher, A.; Heinrich, C.A. Fluid-fluid interactions in Earth's lithosphere. *Rev. Mineral. Geochem.* **2007**, *65*, 1–13. [[CrossRef](#)]
4. Zhang, D.H.; Jin, X.D.; Mao, S.D.; Wang, L.L. The classification of ore-forming fluid and the efficiency of ore formation of magmatic hydrothermal solution. *Earth Sci. Front.* **2011**, *18*, 90–102, (In Chinese with English Abstract).
5. Kucha, H.; Schroll, E.; Raith, J.; Halas, S. Microbial sphalerite formation in carbonate-hosted Zn-Pb ores, Bleiberg, Austria: Micro-to nanotextural and sulfur isotope evidence. *Econ. Geol.* **2010**, *105*, 1005–1023. [[CrossRef](#)]
6. Leach, D.L.; Bradley, D.C.; Lewchuk, M.; Symons, D.T.A.; Brannon, J.; Marsily, G. Mississippi Valley-type lead-zinc deposits through geological time: Implications from recent age-dating research. *Miner. Depos.* **2001**, *36*, 711–740. [[CrossRef](#)]
7. Wilkinson, J.J.; Weiss, D.J.; Mason, T.; Coles, B.J. Zinc isotope variation in hydrothermal systems: Preliminary evidence from the Irish Midlands ore field. *Econ. Geol.* **2005**, *100*, 583–590. [[CrossRef](#)]
8. Höll, R.; Kling, M.; Schroll, E. Metallogenesis of germanium—A review. *Ore Geol. Rev.* **2007**, *30*, 145–180. [[CrossRef](#)]
9. Han, R.S.; Zhang, Y.; Ren, T.; Qiu, W.L.; Wei, T.P. A summary of research on carbonate-hosted, non-magmatic, epigenetic, hydrothermal type Pb-Zn deposits. *J. Kunming Univ. Sci. Technol. (Nat. Sci.)* **2020**, *45*, 29–40. (In Chinese with English Abstract)
10. Giorno, M.; Barale, L.; Bertok, C.; Frenzel, M.; Looser, N.; Guillong, M.; Bernasconi, S.M.; Martire, L. Sulfide-associated hydrothermal dolomite and calcite reveal a shallow burial depth for Alpine-type Zn-(Pb) deposits. *Geology* **2022**, *50*, 853–858. [[CrossRef](#)]
11. Sangster, D.F. Mississippi Valley-type and SEDEX lead-zinc deposits: A comparative examination. *Trans. Inst. Min. Metall.* **1990**, *99*, B21–B42.
12. Leach, D.L.; Sangster, D.F. Mississippi Valley-type lead-zinc deposits. In *Mineral Deposit Modelling*; Special Paper 40; Kirkham, R.V., Sinclair, W.D., Thorpe, R.L., Duke, J.M., Eds.; Geological Association of Canada: St. John's, NL, Canada, 1993; pp. 289–314.
13. Leach, D.L.; Sangster, D.F.; Kelley, K.D.; Large, R.R.; Walters, S.G. Sediment-host lead-zinc deposits: A global perspective. *Econ. Geol.* **2005**, *100*, 561–607.
14. Kesler, S.E.; Martini, A.M.; Appold, M.S.; Walter, L.M.; Huston, Y.J.; Furman, F.C. Na-Cl-Br systematics of fluid inclusions from Mississippi Valley-type deposits, Appalachian Basin: Constraints on solute origin and migration paths. *Geochim. Cosmochim. Acta* **1996**, *60*, 225–233. [[CrossRef](#)]
15. Liu, H.C.; Lin, W.D. *Regularity Research of Lead-Zinc-Silver Deposits in Northeastern Yunnan Province*; Yunnan University Press: Kunming, China, 1999; pp. 1–468. (In Chinese)
16. Huang, Z.L.; Chen, J.; Han, R.S.; Li, W.B.; Liu, C.Q.; Zhang, Z.L.; Ma, D.Y.; Gao, D.R.; Yang, H.L. *Geochemistry and Ore-Formation of the Huize Giant Lead-Zinc Deposit, Yunnan Province, China: Discussion on the Relationship between the Emeishan Flood Basalts and Lead-Zinc Mineralization*; Geological Publishing House: Beijing, China, 2004; pp. 1–214. (In Chinese)
17. Zhou, J.X.; Huang, Z.L.; Gao, J.G.; Yan, Z.F. Geological and C-O-S-Pb-Sr isotopic constraints on the origin of the Qingshan carbonate-hosted Pb-Zn deposit, Southwest China. *Int. Geol. Rev.* **2013**, *55*, 904–916. [[CrossRef](#)]
18. Zhou, J.X.; Xiang, Z.Z.; Zhou, M.F.; Feng, Y.X.; Luo, K.; Huang, Z.L.; Wu, T. The giant Upper Yangtze Pb-Zn province in SW China: Reviews, new advances and a new genetic model. *J. Asian Earth Sci.* **2018**, *154*, 280–315. [[CrossRef](#)]
19. Zhang, Y.; Han, R.S.; Ding, X.; Wang, Y.R.; Wei, T.P. Experimental study on fluid migration mechanism related to Pb-Zn super-enrichment: Implications for mineralization mechanisms of the Pb-Zn deposits in the Sichuan-Yunnan-Guizhou, SW China. *Ore Geol. Rev.* **2019**, *114*, 103110. [[CrossRef](#)]
20. Han, R.S.; Zhang, Y.; Wang, F.; Wu, P.; Qiu, W.L.; Li, W.Y. *Metallogenic Mechanism of Germanium Rich Lead-Zinc Deposits and Prediction of Concealed Ore Location in Northeast Yunnan*; Science Press: Beijing, China, 2019; pp. 1–501. (In Chinese with English Abstract)
21. Han, R.S.; Wu, P.; Zhang, Y.; Huang, Z.L.; Wang, F.; Jin, Z.G.; Zhou, G.M.; Shi, Z.L.; Zhang, C.Q. New research progresses of metallogenic theory for rich Zn-Pb-(Ag-Ge) deposits in the Sichuan-Yunnan-Guizhou Triangle (SYGT) area, southwestern Tethys. *Acta Geol. Sin.* **2022**, *96*, 554–573. (In Chinese with English Abstract)
22. Ye, L.; Cook, N.J.; Ciobanu, C.L.; Liu, Y.P.; Zhang, Q.; Liu, T.G.; Wei, G.; Yang, Y.L.; Danyushevskiy, L. Trace and minor elements in sphalerite from base metal deposits in South China: A LA-ICPMS study. *Ore Geol. Rev.* **2011**, *39*, 188–217. [[CrossRef](#)]
23. Zhang, C.Q.; Xu, J.J.; Mao, J.W.; Rui, Z.Y. Advances in the study of Mississippi Valley-type deposits. *Miner. Depos.* **2009**, *28*, 195–210. (In Chinese with English Abstract)
24. Zhang, C.Q.; Wu, Y.; Hou, L.; Mao, J.W. Geodynamic setting of mineralization of Mississippi Valley-type deposits in world-class Sichuan-Yunnan-Guizhou Zn-Pb triangle, southwest China: Implications from age-dating studies in the past decade and the Sm-Nd age of the Jinshachang deposit. *J. Asian Earth Sci.* **2015**, *103*, 103–114. [[CrossRef](#)]
25. Leach, D.L.; Song, Y.C. Sediment-hosted zinc-lead copper deposits in China. In *Mineral Deposits of China*; Special Publication Number, 22; Chang, Z., Goldfarb, R.J., Eds.; Society of Economic Geologist, Inc.: Lawrence, KS, USA, 2019; pp. 325–409.

26. Han, R.S.; Hu, Y.Z.; Wang, X.K.; Hou, B.H.; Huang, Z.L.; Chen, J.; Wang, F.; Wu, P.; Li, B.; Wang, H.J.; et al. Mineralization model of rich Ge-Ag-bearing Zn-Pb polymetallic deposit concentrated district in northeastern Yunnan, China. *Acta Geol. Sin.* **2012**, *86*, 280–294. (In Chinese with English Abstract)
27. Han, R.S.; Wang, F.; Hu, Y.Z.; Wang, X.K.; Ren, T.; Qiu, W.L.; Zhong, K.H. Metallogenic tectonic dynamics and chronology constrains on the Huize-type (HZZ) germanium-rich silver-zinc-lead deposits. *Geotecton. Metallog.* **2014**, *38*, 759–771. (In Chinese with English Abstract)
28. Han, R.S.; Chen, J.; Wang, F.; Wang, X.K.; Li, Y. Analysis of metal-element association halos within fault zones for the exploration of concealed ore-bodies—A case study of the Qilinchang Zn-Pb-(Ag-Ge) deposit in the Huize mine district, northeastern Yunnan, China. *J. Geochem. Explor.* **2015**, *159*, 62–78. [[CrossRef](#)]
29. Han, R.S.; Zhang, Y.; Qiu, W.L.; Ding, T.Z.; Wang, M.Z.; Wang, F. Geology and geochemistry of Zn-Pb-(Ge-Ag) deposits in the Sichuan-Yunnan-Guizhou Triangle area, China: A review and a new type. *Front. Earth Sci.* **2023**, *11*, 1136397. [[CrossRef](#)]
30. Zhou, J.X.; Huang, Z.L.; Yan, Z.F. The origin of the Maozu carbonate-hosted Pb-Zn deposits, southwest China: Constrained by C-O-S-Pb isotopic compositions and Sm-Nd isotopic age. *J. Asian Earth Sci.* **2013**, *73*, 39–47. [[CrossRef](#)]
31. Xu, Y.; Huang, Z.L.; Zhu, D.; Luo, T.Y. Origin of hydrothermal deposits related to the Emeishan magmatism. *Ore Geol. Rev.* **2014**, *63*, 1–8. [[CrossRef](#)]
32. Qiu, Y.M.; Gao, S.; McNaughton, N.J.; Groves, D.I.; Ling, W.L. First evidence of > 3.2Ga continental crust in the Yangtze craton of South China and its implications for Archean crustal evolution and Phanerozoic tectonics. *Geology* **2000**, *28*, 11–14. [[CrossRef](#)]
33. Gao, S.; Yang, J.; Zhou, L.; Li, M.; Hu, Z.; Guo, J.; Yuan, H.; Gong, H.; Xiao, G.; Wei, J. Age and growth of the Archean Kongling terrain, South China, with emphasis on 3.3 Ga granitoid gneisses. *Am. J. Sci.* **2011**, *311*, 153–182. [[CrossRef](#)]
34. Zhao, X.F.; Zhou, M.F.; Li, J.W.; Sun, M.; Gao, J.F.; Sun, W.H.; Yang, J.H. Late Paleoproterozoic to Early Mesoproterozoic Dongchuan Group in Yunnan, SW China: Implications for tectonic evolution of the Yangtze Block. *Precambrian Res.* **2010**, *182*, 57–69. [[CrossRef](#)]
35. Sun, W.H.; Zhou, M.F.; Yan, D.P.; Li, J.W.; Ma, Y.X. Provenance and tectonic setting of the Neoproterozoic Yanbian group, western Yangtze block (SW China). *Precambrian Res.* **2008**, *167*, 213–236. [[CrossRef](#)]
36. Wang, L.J.; Yu, J.H.; Griffin, W.L.; O'Reilly, S.Y. Early crustal evolution in the western Yangtze Block: Evidence from U-Pb and Lu-Hf isotopes on detrital zircons from sedimentary rocks. *Precambrian Res.* **2012**, *222*, 368–385. [[CrossRef](#)]
37. Zhou, M.F.; Malpas, J.; Song, X.Y.; Robinsin, P.T.; Sun, M.; Kennedy, K.K.; Leher, C.M.; Keays, R.R. At temporal link between the Emeishan large igneous province (SW China) and the end-Guadalupian mass extinction. *Earth Planet. Sci. Lett.* **2002**, *196*, 113–122. [[CrossRef](#)]
38. Luo, K.; Zhou, J.X.; Huang, Z.L.; Wang, X.K.; Wilde, S.A.; Zhou, W.; Tian, L.Y. New insights into the origin of early Cambrian carbonate-hosted Pb-Zn deposits in South China: A case study of the Maliping Pb-Zn deposit. *Gondwana Res.* **2019**, *70*, 88–103. [[CrossRef](#)]
39. Wang, Q.F.; Yang, L.; Xu, X.J.; Santosh, M.; Wang, Y.N.; Wang, T.Y.; Chen, F.G.; Wang, R.X.; Gao, L.; Liu, X.F.; et al. Multi-stage tectonics and metallogeny associated with Phanerozoic evolution of the South China Block: A holistic perspective from the Youjiang Basin. *Earth-Sci. Rev.* **2020**, *211*, 103405. [[CrossRef](#)]
40. Luo, K.; Zhou, J.X.; Ju, Y.W. A shift from BSR to TSR caused the formation of the Chipu Pb-Zn deposit, South China. *Ore Geol. Rev.* **2022**, *144*, 104845. [[CrossRef](#)]
41. Zhou, J.X.; Bai, J.H.; Huang, Z.L.; Zhu, D.; Yan, Z.F.; Lv, Z.C. Geology, isotope geochemistry and geochronology of the Jinshachang carbonate-hosted Pb-Zn deposit, southwest China. *J. Asian Earth Sci.* **2015**, *98*, 272–284. [[CrossRef](#)]
42. Ren, T.; Zhou, J.X.; Wang, D.; Yang, G.S.; Lv, C.L. Trace elemental and S-Pb isotopic geochemistry of the Fule Pb-Zn deposit, NE Yunnan Province. *Acta Petrol. Sin.* **2019**, *35*, 3493–3505. (In Chinese with English Abstract)
43. Li, Z.L.; Ye, L.; Hu, Y.S.; Wei, C.; Huang, Z.L.; Yang, Y.L.; Danyushevsky, L. Trace elements in sulfides from the Maozu Pb-Zn deposit, Yunnan Province, China: Implications for trace-element incorporation mechanisms and ore genesis. *Am. Mineral.* **2020**, *105*, 1734–1751. [[CrossRef](#)]
44. Zhao, D.; Han, R.; Wang, L.; Ren, T.; Wang, J.S.; Zhang, X.P. Genesis of the Lehong large zinc-lead deposit in northeastern Yunnan, China: Evidences from geological characteristics and C-H-O-S-Pb isotopic compositions. *Ore Geol. Rev.* **2021**, *135*, 104219. [[CrossRef](#)]
45. Wei, A.Y.; Xue, C.D.; Xiang, K.; Li, J.; Liao, C.; Akhter, Q.J. The ore-forming process of the Maoping Pb-Zn deposit, northeastern Yunnan, China: Constraints from cathodoluminescence (CL) petrography of hydrothermal dolomite. *Ore Geol. Rev.* **2015**, *70*, 562–577. [[CrossRef](#)]
46. Xiang, Z.Z.; Zhou, J.X.; Luo, K. New insights into the multi-layer metallogenesis of carbonated-hosted epigenetic Pb-Zn deposits: A case study of the Maoping Pb-Zn deposit, South China. *Ore Geol. Rev.* **2020**, *122*, 103538. [[CrossRef](#)]
47. Han, R.S.; Wu, P.; Wang, F.; Zhou, G.M.; Li, W.Y.; Qiu, W.L. 'Four Steps Type' ore-prospecting method for deeply concealed hydrothermal ore deposits—A case study of the Maoping Zn-Pb-(Ag-Ge) deposit in Southwestern China. *Geotecton. Metallog.* **2019**, *43*, 246–257. (In Chinese with English Abstract)
48. Yang, Q.; Liu, W.H.; Zhang, J.; Wang, J.; Zhang, X.J. Formation of Pb-Zn dposits in the Sichuan-Yunnan-Guizhou triangle linked to the Youjiang foreland basin: Evidence from Rb-Sr age and in situ sulfur isotope analysis of the Maoping Pb-Zn deposit in northeastern Yunnan Province, southeast China. *Ore Geol. Rev.* **2019**, *107*, 780–800. [[CrossRef](#)]

49. Tan, S.C.; Zhou, J.X.; Luo, K.; Xiang, Z.Z.; He, X.H.; Zhang, Y.H. The sources of ore-forming elements of the Maoping large-scale Pb-Zn deposit, Yunnan Province: Constrains from in-situ S and Pb isotopes. *Acta Petrol. Sin.* **2019**, *35*, 3461–3476. (In Chinese with English Abstract)
50. Hu, X.Y.; Chen, Y.H.; Liu, G.X.; Yang, H.; Luo, J.H.; Ren, K.Y.; Yang, Y.G. Numerical modeling of formation of the Maoping Pb-Zn deposit within the Sichuan-Yunnan-Guizhou Metallogenic Province, Southwestern China: Implications for the spatial distribution of concealed Pb mineralization and its controlling factors. *Ore Geol. Rev.* **2022**, *140*, 104573. [[CrossRef](#)]
51. Wang, L.; Han, R.S.; Zhang, Y.; Zhou, G.M.; Zhong, H.; Zuo, J.G.; Deng, P. Spatial structure orebodies and prediction of deep orebodies of Maoping lead-zinc deposit, northeastern Yunnan Province. *Miner. Depos.* **2022**, *41*, 207–224. (In Chinese with English Abstract)
52. Wei, C.; Ye, L.; Hu, Y.S.; Huang, Z.L.; Danyushevsky, L.; Wang, H.Y. LA-ICP-MS analyses of trace elements in base metal sulfides from carbonate-hosted Zn-Pb deposits, South China: A case study of the Maoping deposit. *Ore Geol. Rev.* **2021**, *130*, 103945. [[CrossRef](#)]
53. Roedder, E. Fluid inclusions. *Rev. Mineral.* **1984**, *12*, 644.
54. Lu, H.Z.; Fan, H.R.; Ni, P.; Ou, G.X.; Shen, K.; Zhang, W.H. *Fluid Inclusions*; Science Press: Beijing, China, 2004; pp. 1–487. (In Chinese)
55. Bauer, M.E.; Burisch, M.; Ostendorf, J.; Krause, J.; Frenzel, M.; Seifert, T.; Gutzmer, J. Trace element geochemistry of sphalerite in contrasting hydrothermal fluid systems of the Freiberg district, Germany: Insights from LA-ICP-MS analysis, near-infrared light microthermometry of sphalerite-hosted fluid inclusions, and sulfur isotope geochemistry. *Miner. Depos.* **2019**, *54*, 237–262.
56. Bodnar, R.J. Revised equation and table for determining the freezing point depression of H₂O-NaCl solutions. *Geochim. Cosmochim. Acta* **1993**, *57*, 683–684. [[CrossRef](#)]
57. Matsuda, J.; Matsumoto, T.; Sumino, H.; Nagao, K.; Yamamoto, J.; Miura, Y.; Kaneoka, I.; Takahata, N.; Sano, Y. The ³He/⁴He ratio of the new internal He standard of Japan (HESJ). *Geochem. J.* **2002**, *36*, 191–195. [[CrossRef](#)]
58. He, H.Y.; Zhu, R.X.; Saxton, J. Noble gas isotopes in corundum and peridotite xenoliths from the eastern North China Craton: Implication for comprehensive refertilization of lithospheric mantle. *Phys. Earth Planet Inter.* **2011**, *189*, 185–191. [[CrossRef](#)]
59. Zhang, P.; Kou, L.L.; Zhao, Y.; Sha, D.M. Genesis of the Maoling gold deposit in the Liaodong Peninsula: Constraints from a combined fluid inclusion, C-H-O-S-Pb-He-Ar isotopic and geochronological studies. *Geosci. Front.* **2022**, *13*, 101379. [[CrossRef](#)]
60. O’Neil, J.R.; Clayton, R.N.; Mayeda, T.K. Oxygen isotope fractionation in divalent metal carbonates. *J. Chem. Phys.* **1969**, *51*, 5547–5558. [[CrossRef](#)]
61. Stuart, F.M.; Burnard, P.G.; Taylor, R.P.; Turner, G. Resolving mantle and crustal contributions to ancient hydrothermal fluids: He-Ar isotopes in fluid inclusions from Dae Hwa W-Mo mineralization, South Korea. *Geochim. Cosmochim. Acta* **1995**, *59*, 4663–4673. [[CrossRef](#)]
62. Burnard, P.G.; Hu, R.; Turner, G.; Bi, X.W. Mantle, crustal and atmospheric noble gases in Ailaoshan Gold deposits, Yunnan Province, China. *Geochim. Et Cosmochim. Acta* **1999**, *63*, 1595–1604. [[CrossRef](#)]
63. Liu, J.C.; Wang, Y.T.; Hu, Q.Q.; Wei, R.; Huang, S.K.; Sun, Z.H.; Hao, J.L. Ore genesis of the Fancha gold deposit, Xiaolinling goldfield, southern margin of the North China Craton: Constraints from pyrite Re-Os geochronology and He-Ar, in-situ S-Pb isotopes. *Ore Geol. Rev.* **2020**, *119*, 103373. [[CrossRef](#)]
64. Yu, D.S.; Xu, D.R.; Wang, Z.L.; Xu, K.; Huang, Q.Y.; Zou, S.H.; Zhao, Z.X.; Deng, T. Trace element geochemistry and O-S-Pb-He-Ar isotopic systematics of the Lishan Pb-Zn-Cu hydrothermal deposit, NE Hunan, South China. *Ore Geol. Rev.* **2021**, *133*, 104091. [[CrossRef](#)]
65. Gao, Y.; Liu, J.; Li, T.G.; Zhang, D.D.; Yang, Y.C.; Han, S.J.; Ding, Q.F.; Zhang, S. Multiple isotope (He-Ar-Zn-Sr-Nd-Pb) constraints on the genesis of the Jiawula Pb-Zn-Ag deposit, NE China. *Ore Geol. Rev.* **2021**, *134*, 104142. [[CrossRef](#)]
66. Kendrick, M.A.; Burgess, R.; Patrick, R.A.D.; Turner, G. Fluid inclusion noble gas and halogen evidence on the origin of Cu-porphyry mineralizing fluids. *Geochim. Cosmochim. Acta* **2001**, *65*, 2651–2668. [[CrossRef](#)]
67. Wilkinson, J.J. A review of fluid inclusion constraints on mineralization in the Irish ore field and implications for the genesis of sediment-hosted Zn-Pb deposits. *Econ. Geol.* **2010**, *105*, 417–442. [[CrossRef](#)]
68. Han, R.S.; Li, B.; Ni, P.; Qiu, W.L.; Wang, X.D.; Wang, T.G. Infrared micro-thermometry of fluid inclusions in sphalerite and geological significance of Huize super-lager Zn-Pb-(Ge-Ag) deposit, Yunnan Province. *J. Jilin Univ. (Earth Sci. Ed.)* **2016**, *46*, 91–104. (In Chinese with English Abstract)
69. Wang, J.; Zhang, J.; Zhong, W.B.; Yang, Q.; Li, F.K.; Zhu, Z.K. Sources of ore-forming fluids from Tianbaoshan and Huize Pb-Zn deposits in Yunnan-Sichuan-Guizhou region, Southwest China: Evidence from fluid inclusions and He-Ar isotopes. *Earth Sci.* **2018**, *43*, 2076–2099. (In Chinese with English Abstract)
70. Burruss, R.C. Diagenetic palaeotemperatures from aqueous fluid inclusions: Re-equilibration of inclusions in carbonate cements by burial heating. *Mineral. Mag.* **1987**, *51*, 477–481. [[CrossRef](#)]
71. Bodnar, R.J.; Binns, P.R.; Hall, D.L. Synthetic fluid inclusions. VI. Quantitative evaluation of the decrepitation behavior of fluid inclusions in quartz at one atmosphere confining pressure. *J. Metamorph. Geol.* **1980**, *7*, 229–242. [[CrossRef](#)]
72. Li, D.F.; Chen, H.Y.; Zhang, L.; Hollings, P.; Chen, Y.J.; Lu, W.J.; Zheng, Y.; Wang, C.M.; Fang, J.; Chen, G.; et al. Ore geology and fluid evolution of the giant Caixiashan carbonate-hosted Zn-Pb deposit in the Eastern Tianshan, NW China. *Ore Geol. Rev.* **2016**, *72*, 355–372. [[CrossRef](#)]

73. Nejadhadad, M.; Taghipour, B.; Lentz, D.R. Implications of multiple fluids in the deposition of Pb-Zn-Ba deposits in the Alvand Mountain, Golpayegan, Iran: Evidence from fluid inclusions and O, C, S isotopes. *Ore Geol. Rev.* **2023**, *153*, 105300. [[CrossRef](#)]
74. Taylor, H.P. The application of oxygen and hydrogen isotope studies to problems of hydrothermal alteration and ore deposition. *Econ. Geol.* **1974**, *69*, 843–883. [[CrossRef](#)]
75. Samson, I.M.; Russell, M.J. Genesis of the Silvermines zinc-lead-barite deposit, Ireland: Fluid inclusion and stable isotope evidence. *Econ. Geol.* **1987**, *82*, 371–394. [[CrossRef](#)]
76. Kesler, S.E.; Vennemann, T.W.; Frederickson, C.; Breithaupt, A.; Vazquez, R.; Furman, F.C. Hydrogen and oxygen isotope evidence for origin of MVT-forming brines, southern Appalachians. *Geochim. Cosmochim. Acta* **1997**, *61*, 1513–1523. [[CrossRef](#)]
77. Meinert, L.D.; Hedenquist, J.W.; Satoh, H.; Matsuhisa, Y. Formation of anhydrous and hydrous skarn in Cu-Au ore deposits by magmatic fluids. *Econ. Geol.* **2003**, *98*, 147–156. [[CrossRef](#)]
78. Xu, R.; Li, W.C.; Deng, M.G.; Zhou, J.X.; Ren, T.; Yu, H.J. Genesis of the superlarge Luziyuan Zn-Pb-Fe(-Cu) distal skarn deposit in western Yunnan (SW China): Insights from ore geology and C-H-O-S isotopes. *Ore Geol. Rev.* **2019**, *107*, 944–959. [[CrossRef](#)]
79. Wang, K.; Wang, Y.H.; Xue, C.J.; Liu, J.J.; Zhang, F.F. Fluid inclusions and C-H-O-S-Pb isotope systematics of the Caixiashan sediment-hosted Zn-Pb deposit, eastern Tianshan, northwest China: Implication for ore genesis. *Ore Geol. Rev.* **2020**, *119*, 103404. [[CrossRef](#)]
80. Hu, R.Z.; Burnard, P.G.; Bi, X.W.; Zhou, M.F.; Pen, J.T.; Su, W.C.; Wu, K.X. Helium and argon isotope geochemistry of alkaline intrusion-associated gold and copper deposits along the Red River-Jinshajiang fault belt, SW China. *Chem. Geol.* **2004**, *203*, 305–317. [[CrossRef](#)]
81. Hu, R.Z.; Bi, X.W.; Jiang, G.H.; Chen, H.W.; Peng, J.T.; Qi, Y.Q.; Wu, L.Y.; Wei, W.F. Mantle-derived noble gases in ore-forming fluids of the granite-related Yaogangxian tungsten deposit, Southeastern China. *Miner. Depos.* **2012**, *47*, 623–632. [[CrossRef](#)]
82. Kendrick, M.A.; Burnard, P.G. Noble gases and halogens in fluid inclusions: A journey through the earth's crust. In *The Noble Gases as Geochemical Tracers*; Burnard, P.G., Ed.; Springer: Heidelberg, Germany, 2013; pp. 319–369.
83. Bouabdellah, M.; Niedermann, S.; Velasco, F. The Touissit-Bou Bekker Mississippi Valley-Type District of Northeastern Morocco: Relationships to the Messinian salinity crisis, Late Neogene-Quaternary Alkaline magmatism, and buoyancy-driven fluid convection. *Econ. Geol.* **2015**, *110*, 1455–1484. [[CrossRef](#)]
84. Mamyin, B.A.; Tolstikhin, I.N. *Helium Isotopes in Nature*; Elsevier: Amsterdam, The Netherlands, 1984; p. 273.
85. Yang, J.H.; Cawood, P.A.; Du, Y.S.; Huang, H.; Hu, L.S. Detrital record of Indosinian mountain building in SW China: Provenance of the Middle Triassic turbidites in the Youjiang Basin. *Tectonophysics* **2012**, *574*, 105–117. [[CrossRef](#)]
86. Liu, Y.; Hu, K.; Han, S.C.; Sun, Z.H. Structural evolution of the Youjiang Basin and its controlling effects on the formation of Carlin-type gold deposits. *Geol. J. China Univ.* **2015**, *21*, 1–14. (In Chinese with English Abstract)
87. Liu, W.H.; Zhang, J.; Wang, J. Sulfur isotope analysis of carbonate-hosted Zn-Pb deposits in Northwestern Guizhou Province, Southwest China: Implications for the source of reduced sulfur. *J. Geochem. Explor.* **2017**, *181*, 31–44. [[CrossRef](#)]
88. Luo, H.Z. A regressive correlation between volatility and reflectance of vitrinite in the coal beds in Upper Permian formations in Dian-Qian-Gui region and a discussion on their degree of metamorphism. *Pet. Explor. Dev.* **1983**, *6*, 43–50. (In Chinese with English Abstract)
89. Zhuang, X.G. The paleogeothermal field of northwestern Guangxi: Characteristics and its role in the formation of micro-disseminated gold deposits. *Miner. Depos.* **1995**, *14*, 83–89. (In Chinese with English Abstract)
90. DIPG (Dian-Qian-Gui Institute of Petroleum Geology). Research Report on Oil Potential of the Stratum of Yunnan-Guizhou-Guangxi Border Area. 1983; unpublished. (In Chinese)
91. Hitzman, M.W.; Beaty, D.W. The Irish Zn-Pb-(Ba) ore field. *Soc. Econ. Geol. Spec. Publ.* **1996**, *4*, 112–143.
92. Reed, C.P.; Wallace, M.W. Diagenetic evidence for an epigenetic origin of the Courtbrown Zn-Pb deposit, Ireland. *Miner. Depos.* **2001**, *36*, 428–441. [[CrossRef](#)]
93. Li, J.H.; Zhang, Y.Q.; Dong, S.W.; Johnston, S.T. Cretaceous tectonic evolution of South China: A preliminary synthesis. *Earth-Sci. Rev.* **2014**, *134*, 98–136. [[CrossRef](#)]
94. Wu, T.; Huang, Z.L.; He, Y.F.; Yang, M.; Fan, H.F.; Wei, C.; Ye, L.; Hu, Y.S.; Xiang, Z.Z.; Lai, C. Metal source and ore-forming process of the Maoping carbonate-hosted Pb-Zn deposit in Yunnan, SW China: Evidence from deposit geology and sphalerite Pb-Zn-Cd isotopes. *Ore Geol. Rev.* **2021**, *135*, 104214. [[CrossRef](#)]
95. Wang, C.; Bagas, L.; Lu, Y.; Santosh, M.; Du, B.; McCuaig, T.C. Terrane boundary and spatio-temporal distribution of ore deposits in the Sanjiang Tethyan Orogen: Insights from zircon Hf-isotopic mapping. *Earth-Sci. Rev.* **2016**, *156*, 39–65. [[CrossRef](#)]
96. Wu, Y.; Kong, Z.G.; Chen, M.H.; Zhang, C.Q.; Cao, L.; Tang, Y.J.; Yuan, X.; Zhang, P. Trace elements in sphalerites from the Mississippi Valley-type lead-zinc deposits around the margins of Yangtze Block and its geological implications: A LAICPMS study. *Acta Petrol. Sin.* **2019**, *35*, 3443–3460. (In Chinese with English Abstract)
97. Liu, X.K.; Chen, F.C.; Chang, H.; Gao, J.G.; Wu, P.; Tan, J. The mineralization of Daxiao carbonate-hosted Pb-Zn deposit, northeast Yunnan province, SW China: Constraints from Rb-Sr isotopic dating and H-O-S-Pb isotopes. *Ore Geol. Rev.* **2022**, *147*, 104956. [[CrossRef](#)]
98. Ren, S.L.; Li, Y.H.; Zeng, P.S.; Qiu, W.L.; Fan, C.F.; Hu, G.Y. Effect of sulfate evaporate salt layer in mineralization of the Huize and Maoping lead-zinc deposits in Yunnan: Evidence from sulfur isotope. *Acta Geol. Sin.* **2018**, *92*, 1041–1055. (In Chinese with English Abstract)

99. Zhang, C.Q.; Mao, J.W.; Yu, J.J.; Li, H.M. Study on fluid inclusion and the metallogenetic mechanism of Chipu Pb-Zn deposit in Sichuan, China. *Acta Petrol. Sin.* **2007**, *23*, 2541–2552. (In Chinese with English Abstract)
100. Zhao, D.; Han, R.S.; Ren, T.; Wang, J.S.; Wu, H.Z.; Zhang, X.P.; Cui, J.H. Characteristics of fluid inclusions geochemistry of Lehong large-sized Pb-Zn ore deposit, northeastern Yunnan Province. *Miner. Depos.* **2018**, *37*, 1018–1036. (In Chinese with English Abstract)
101. Wang, H. Metallogenetic of MVT Lead-Zinc Deposits in Huili-Huidong, Sichuan Province: A Case Study of Daliangzi and Tianbaoshan Pb-Zn Deposits. Ph.D. Dissertation, Kunming University of Science and Technology, Kunming, China, 2019; pp. 1–140. (In Chinese with English Abstract)
102. Yang, Q. Study on Mineralization of Lead-Zinc Deposits in Northeastern Yunnan and Northwestern Guizhou Province, China. Ph.D. Dissertation, China University of Geosciences, Wuhan, China, 2021; pp. 1–183. (In Chinese with English Abstract)
103. Wang, H.; Zhu, X.Y.; Wang, J.B.; Jia, D.L.; Shi, Y.; Chen, L.; Xu, Z.F. Sources of metallogenetic materials and metallogenetic mechanism of Tianbaoshan Pb-Zn deposit in Sichuan Province: Constraints from fluid inclusions and isotopic evidences. *Acta Petrol. Sin.* **2021**, *37*, 1830–1846. (In Chinese with English Abstract)
104. Ding, W.P.; Xie, C.F.; Huang, C.; Zhang, B.; Xin, Z.; Zhan, H.S.; Zheng, L.L.; Kong, F.Q.; Wang, H.B.; Huang, L.F. Sources of Permian lead-zinc ore-forming materials in Sichuan-Yunnan-Guizhou area: C-H-O-S-Pb isotope constraint—An example from Taipingzi lead-zinc deposit in Yunnan Provinces. *Geol. China* **2022**, *49*, 1845–1861. (In Chinese with English Abstract)
105. Wang, G.Z.; Hu, R.Z.; Su, W.C.; Zhu, L.M. Basin fluid flow and mineralization in Youjiang Basin, Yunnan-Guizhou-Guangxi Provinces. *Sci. China (Ser. D)* **2003**, *46*, 99–109.
106. Li, W.B.; Huang, Z.L.; Zhang, G. Sources of the ore metals of the Huize ore field in Yunnan province: Constraints from Pb, S, C, H, O and Sr isotope geochemistry. *Acta Petrol. Sin.* **2006**, *22*, 2567–2580. (In Chinese with English Abstract)
107. Wu, Y.; Zhang, C.Q.; Mao, J.W.; Ouyang, H.G.; Sun, J. The genetic relationship between hydrocarbon systems and Mississippi Valley-type Zn-Pb deposits along the SW margin of Sichuan Basin, China. *Int. Geol. Rev.* **2012**, *55*, 941–957. [[CrossRef](#)]
108. Yuan, B.; Mao, J.W.; Yan, X.H.; Wu, Y.; Zhang, F.; Zhao, L.L. Sources of metallogenetic materials and metallogenetic mechanism of Daliangzi Ore Field in Sichuan Province: Constraints from geochemistry of S, C, H, O, Sr isotope and trace element in sphalerite. *Acta Petrol. Sin.* **2014**, *30*, 209–220. (In Chinese with English Abstract)
109. Yang, Q.; Zhang, J.; Wang, J.; Zhong, W.B.; Liu, W.H. Study of ore-forming fluid geochemistry of Maozu large-scale lead-zinc deposit in northeast Yunnan. *Miner. Resour. Geol.* **2017**, *31*, 854–863. (In Chinese with English Abstract)
110. Anderson, G.M. Precipitation of Mississippi Valley-type ores. *Econ. Geol.* **1975**, *70*, 937–942. [[CrossRef](#)]
111. Symons, D.A. Genesis of Mississippi Valley-type lead-zinc deposits. *Annu. Rev. Earth Planet. Sci.* **1986**, *14*, 177–199.
112. Barton, P.B. Possible role of organic matter in the precipitation of the Mississippi Valley ores: Genesis of strata-bound lead-zinc-barite-fluorite deposits in carbonate rocks. *Econ. Geol. Monogr.* **1967**, *3*, 371–377.
113. Anderson, G.M. Organic maturation and ore precipitation in Southeast Missouri. *Econ. Geol.* **1991**, *86*, 909–926. [[CrossRef](#)]
114. Corbella, M.; Ayora, C.; Cardellach, E. Hydrothermal mixing, carbonate dissolution and sulfide precipitation in Mississippi Valley-type deposit. *Miner. Depos.* **2004**, *39*, 344–357. [[CrossRef](#)]
115. Anderson, G.M. The mixing hypothesis and the origin of Mississippi Valley-type ore deposits. *Econ. Geol.* **2008**, *103*, 1683–1690. [[CrossRef](#)]
116. Plumlee, G.S.; Leach, D.L.; Hofstra, A.H.; Landis, G.P.; Rowan, E.L.; Viets, J.G. Chemical reaction path modeling of ore deposition in Mississippi Valley-type Pb-Zn deposits of the Ozark region, U.S. midcontinent. *Econ. Geol.* **1994**, *89*, 1361–1383. [[CrossRef](#)]

Disclaimer/Publisher’s Note: The statements, opinions and data contained in all publications are solely those of the individual author(s) and contributor(s) and not of MDPI and/or the editor(s). MDPI and/or the editor(s) disclaim responsibility for any injury to people or property resulting from any ideas, methods, instructions or products referred to in the content.